Impact of Hard Carbon Properties on Their Performance in Potassium-Ion Batteries

Louiza Larbi, Badre Larhrib, Adrian Beda, Lénaïc Madec, Laure Monconduit, Camelia Matei Ghimbeu

Impact of hard carbon properties on their performance in potassium-ion batteries

Louiza LARBI[a,b], Badre LARHRIB[c], Adrian BEDA[a,b,d], Lénaïc MADEC[c,e], Laure MONCONDUIT[d,e,*], Camelia MATEI GHIMBEU[a,b,d,*]

[a] *Université de Haute-Alsace, Institut de Science des Matériaux de Mulhouse (IS2M), CNRS UMR 7361, F-68100 Mulhouse, France*

[b] *Université de Strasbourg, F-67081 Strasbourg, France*

[c] *Universite de Pau et des Pays de l'Adour, E2S UPPA, CNRS, IPREM, 64053 Pau, France*

[d] *Réseau sur le Stockage Electrochimique de l'Energie, CNRS FR3459, Amiens, France*

[e] *ICGM, Univ. Montpellier, CNRS, ENSCM, 34293 Montpellier, France*

Corresponding authors: *E-mails: camelia.ghimbeu@uha.fr; laure.monconduit@umontpellier.fr

Abstract

This work reports on the synthesis of hard carbon spheres (HCS) and the impact of the pyrolysis temperature (1500 to 1900 °C) on the properties of HC and its relationship with the electrochemical performance in potassium-ion batteries (KIBs). Comparison with commercial graphite performance is provides as well. Spherical morphology, disordered structure, and low surface area were obtained for the HCSs. Most properties (interlayer space, active surface area, and oxygen-based functional groups) were found to decrease with increasing pyrolysis temperature, except for the helium density and closed porosity, which increase. However, graphite presents a flake-like morphology with a larger particle size, a higher helium density, an ordered structure with a smaller interlayer distance, and no closed pores. Electrochemical tests in half-cell *vs.* K^+/K showed that HCSs perform better than graphite with higher initial coulombic efficiency (ICE) and better specific capacities. The HCSs pyrolyzed at 1500 and 1700 °C exhibit the best initial Coulombic efficiency, ICE of 54 and 62% and specific capacities of 254 and 247 mAh g^{-1} (C/20, 11.5 mA g^{-1}), respectively. The ICE is affected by multiple surface and bulk parameters, but also by electrolyte formulation (67% for 0.8M KFSI *vs* 62% for 0.8M KPF_6). The capacity is governed by diffusive phenomena, and a larger interlayer graphitic spacing and defects favour a better insertion of K ions. Closed pores did not lead to an improvement in capacity. Furthermore, HCSs exhibit significantly better capacity retention (97%) than graphite (84%) especially when cycled at high current rates (up to 10C depotassiation rate).

Keywords

Hard carbon; Graphite; Anodes; Potassium-ion batteries; Energy storage.

1. Introduction

Since their commercialization in 1990, lithium-ion batteries (LIBs) have been the most common and widely used systems for various applications[1]. They deliver a high energy density with an acceptable lifespan. However, the increased demand for LIBs triggered a consequent lithium consumption and raised concerns about the depletion of lithium resources, which already suffers from a poor abundance and heterogeneous localization over the world. To address this dilemma, the development of new advanced battery systems, as an alternative to LiBs, is strongly required. In this regard, sodium ion batteries (NIBs) have been studied for several years while the attention to potassium ion batteries (KIBs) has only begun recently[2], mainly due to the high natural abundance of Na and K, which could ensure long-term availability, lower cost, and long lasting technology. One of the first works on KIBs was reported in 2004 by Eftekhari *et al.*[3] but KIBs research was only recently extended, as testified by the upward spark in publications[4]. Among the advantages of KIBs, we can cite: i) the similarities between Li and K: both are alkali metals sharing the same chemistry and have a close standard potential; ii) potassium is the seventh abundant element in the Earth crust, nearly 1000 times more abundant than lithium and equally available throughout the world[4,5]; iii) the possibility of using aluminium as a current collector for both electrodes instead of the more expensive copper used for Li anodes. All of these assets should lead to a relative lower cost technology of KIBs than LIBs, with the condition to deliver a longer lifetime than LIBs[6]. As potassium presents a slightly lower standard potential than lithium in the solvents used in electrolytes (PC or EC/DEC), the expected energy density of KIBs will be slightly higher than that of LIBs in a full cell. Furthermore, solvated potassium ions are smaller than lithium due to its weaker Lewis acidity, consequently, solvated K^+ shows higher transport numbers and ionic conductivity[5, 7], so that high-power KIBs are expected.

Despite these positive aspects, potassium presents some issues, such as its higher weight compared to its analogues Li and Na, as well as its larger radius (1.38 Å) compared to lithium (0.76 Å). These limitations may cause volume expansion and poor kinetics limiting the K^+ intercalation in the host electrode materials (*i.e.*, graphite)[8], leading to poor cycling stability and rate capability. Furthermore, the high reactivity of potassium metal with organic electrolytes and the impact of salt anion on K metal reactivity are major inconvenience in half-cells[9]. In recent studies[4,10] it was demonstrated that the potassium metal strongly reacts with different electrolytes and other parts of the cell, causing battery performance degradation (large ohmic resistance and fast electrolyte degradation) and electrode polarisation increases.

Furthermore, the lower melting point of potassium (63.38 °C) *vs.* lithium (180.54 °C) might limit its applicability under certain conditions. These both aspects can cause security problems and need to be considered[4,11].

Several materials were investigated as negative electrodes for KIBs such as carbons (graphite, hard carbon)[12], metal alloys (Sn, Sb, Bi and P based alloys...)[13–15], metal oxides (Fe_xO_y, SnO_2…)[16] and metal sulphides (MoS_2, SnS_2…)[16]. However, carbonaceous materials appear to be the most promising for KIB negative electrodes due to their high electronic conductivity, good chemical stability, eco-friendliness, availability, and low price[17–19]. Jian *et al.*[20] reported that graphite, the most used anode material in LIBs, allows the insertion of K^+ to form KC_8 compound. However, the gravimetric capacity is still lower, *i.e.,* 278 mAh g^{-1} compared to 372 mAh g^{-1} in LIBs with the formation of LiC_6[21]. Furthermore, the formation of intercalated graphite compounds triggers a large volume expansion in KIBs, approximately 61% *vs.* 10% in LIBs, causing capacity fading during the electrochemical cycling and a limited life span of the KIBs[22]. To circumvent this problem, various alternative forms of carbon materials have been studied *i.e.*, commercial expanded graphite[23], heteroatom doped graphene[21], reduced graphene[24], carbon nanofiber[25], carbon-based composite materials, soft carbons and hard carbons (HCs)[26].

Among these materials, hard carbon delivers high electrochemical performance (capacity and cycle life) as anode in both LIBs and NIBs due to its structural stability [14,27,28]. HCs can be obtained from organic precursors, by a simple pyrolysis of biomass[29], resins (phenolic resin, epoxy resin, polyfurfuryl alcohol, etc.)[27,30] and/or biopolymers[31]. HC refers to a carbon material, which does not graphitize even under high temperatures (> 2000 °C) and is characterized by a complex structure. As described by Dahn *et al.*[32] in the "falling cards" model, HCs are composed of a mixture of disordered and graphitic domains with open and closed pores. HCs can thus accommodate the insertion/extraction of large K-ions[33,34]. Furthermore, the disordered structure and the greater graphene interlayer distance of HC *vs.* graphite, limit the volume expansion during K^+ insertion / extraction. In this direction, different approaches have been proposed to overcome the volume expansion and improve the electrochemical performance of HCs in KIBs, especially by focussing on the structure engineering of hard carbons, *i.e.,* by playing on the carbon precursor, developing new synthesis processes, controlling the properties (morphology, structure, texture, functionalities) and active material utilization (electrode formulation). These approaches can help to understand / optimize multiple properties, such as the diffusion efficiency of K-ions, the volume expansion rate, the kinetic

reaction, the contact between the electrolyte and the active materials, and electrochemical properties such as coulombic efficiency (CE) and rate performance[12].

For example, Liu's group reported the impact of structure in K-ion storage by synthesising active hollow nanospheres with a broader graphene interlayer spacing (0.408 nm), at 800°C using scalable self-template strategy, followed by a KOH activation process. The improved structure of the carbon nanospheres after activation resulted in a high initial charge capacity of 370.2 mAh g^{-1} at 0.2 A g^{-1}. Furthermore, *ex-situ* X-ray diffraction (XRD) and transmission electron microscopy (TEM) on post-mortem electrodes (first cycle) showed that a high interlayer spacing can accommodate volume fluctuation and facilitate reversible intercalation of K ions reversible intercalation[18]. However, such material presents a low ICE of 44%. Furthermore, Qiu *et al.*[35] reported the influence of texture on the storage of K ions by synthesizing HC through a pyrolysis process (900, 1000, 1300 and 1500 °C) of a preheated rice husk, followed by a washing step with strong and hazardous acids (HF and HCl). It was noticed that the specific surface area (SSA) decreases (from 365 to 17 m^2 g^{-1}) by increasing the pyrolysis temperature (from 900 to 1500 °C). When tested as anode in KIBs, the sample with the lowest SSA (carbonised at 1500 °C) delivered the best charge capacity and ICE (244 mAh g^{-1}, 49%).

In addition, hydrothermal strategy was reported by Ji *et al.*[31] for the synthesis of HC spheres, using an aqueous solution of sucrose. Narrow and uniform particle sizes were obtained after a pyrolysis step at 1000 °C. The material exhibits an interlayer space of 0.4 nm, SSA of 65 m^2 g^{-1} and a capacity of 262 mAh g^{-1} (at 28 mA g^{-1}) with an ICE of 61.8 %[31]. Moreover, Chen *et al.*[36] reported a carbonization-etching strategy to obtain HC microspheres co-doped with sulfur and oxygen. The material delivered a reversible capacity of 221.3 mAh g^{-1} (at 50 mA g^{-1}) and an ICE of 61%. Although the above-mentioned works present interesting strategies to improve the performance of HC, most of the processes used are difficult to implement and generally require pre-treatments, the addition of activation agents, a chemical washing step, high pressure or high temperature conditions, etc. Moreover, there is a lack of general understanding of the factors that affect both the K ion storage mechanisms and performance.

In this work, we synthesized hard carbon spheres using an environmentally friendly approach (polymerization-precipitation process) in water at room temperature, followed by a pyrolysis step (1500 to 1900 °C), under an atmosphere of argon. Different characterisations were carried out to determine the influence of the pyrolysis temperature on both the physico-chemical properties of the HCS and the electrochemical performance when used as anodes for KIBs. A comparison of electrochemical performance was done with a commercial graphite (Gr-SLP30).

HCSs have been shown to deliver better performance than graphite material, *i.e.,* higher initial CE, higher reversible capacity, and better capacity retention at high rates. This result could be explained by the difference in the structural, textural, and surface chemistry of the materials.

2. Experimental

2.1 Material synthesis

HCSs with controlled particle size and different physico-chemical properties were prepared using an eco-friendly and simple precipitation polymerization method, inspired by our previous works[37,27]. In a typical synthesis (Scheme 1), phloroglucinol (4.1 g) and glyoxylic acid (3.6 g) were dissolved in water (200 mL), under magnetic stirring, followed by the addition of triethylenediamine (TEDA, 1.8 g) as cross-linker. After 15-30 minutes of stirring, this mixture was left to ageing (without stirring) for 24 hours at 25 °C and the solid phenolic resin formed was recovered and dried at 80 °C for 12 hours. Subsequently, the material was pyrolyzed first at 900 °C for 1 hour under argon flow (5 °C min^{-1} heating rate) in an alumina tube furnace and then in a second step at 1500, 1700 and 1900 °C in a graphitic tube furnace. The obtained materials are denoted HCST (where T-indicates the final pyrolysis temperature). The synthesis results in ~ 2.5 - 3 g of carbon / synthesis batch. No grinding is required, which is advantageous for industrial applications. Graphite material called Gr-SLP30 was graciously provided by Timcal (actually called Imerys) and was used without any other modification. It was selected on the basis of its low surface area and active sites, according to our previous study[38], for comparison purposes with hard carbon spheres.

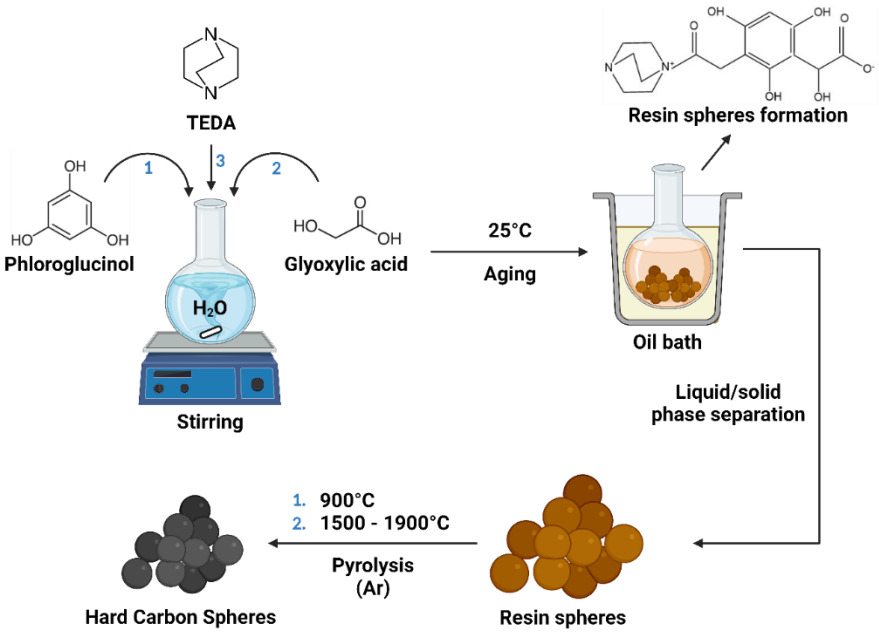

Scheme 1: Schematic representation of the synthesis process of the hard carbon spheres (HCS). Created by authors with BioRender.com.

2.2 Material characterization

The morphology of the obtained HCSs and graphite was observed by scanning electron microscopy (SEM) using FEI Quanta 400 scanning electron microscopy, whereas the particle size distribution was determined by ImageJ software by counting ~ 600 particles of different SEM-images. Structural characterisation of the materials was performed by X-ray diffraction (XRD) using a Burker D8 Advanced diffractometer with flat Bragg-Brentano θ-θ geometry and a copper wavelength of 1.5406 Å. The distance between the graphene planes, $d_{002,}$ was calculated using the graphite diffraction peak (002) and the Bragg equation [39]. The height (L_c) and the width (L_a) of the stacked graphene layers were calculated from the full width at half maximum (FWHM) of the diffraction peaks (002) and (100), respectively, based on Scherrer formula [39].

Raman spectroscopy was performed with a LabRAM BX40 instrument (Horiba Jobin-Yvon) equipped with a He-Ne excitation source (532 nm wavelength). Nine spectra were acquired for each sample by doing a mapping. The average spectrum was used for a good representation of the structure to calculate the I_D/I_G report after fitting with a Gaussian function. Staked graphene plane width (L_a) was calculated by Raman spectroscopy according to the literature[40].The local

structure has been examined by high-resolution microscopy (HRTEM) using a JEOL instrument (ARM-200F model) operating at 200 KV.

Textural characteristics such as specific surface area, SSA (at P/P_0 = 0.01-0.30), total pore volume, V_T (at P/P_0=0.99), and pore size distribution were evaluated with a Micromeritics ASAP 2420 instrument using N_2 adsorbate gas (77 K) and a Micrometrics ASAP 2020 instrument using CO_2 adsorbate gas (273 K) as described elsewhere[41].

Materials density was measured with an Accupyc 1330 pycnometer from Micromeritics working under heliumgas. Before analysis, the materials were first outgazed at 300 °C for 12 hours under vacuum to remove the physisorbed molecules. For each sample, 100 cycles were performed, and the average value of density was taken for every sample. The closed and opened porosity ratios were calculated based on the total pore volume measured by N_2 sorption, and the helium density of HCSs and graphite according to the equations reported in the literature[42,43].

The chemical composition and the functional groups of the HCS surface (3 to 9 nm in thickness) were determined by X-ray photoelectron spectroscopy (XPS) using a SE-2002 (VG SCIENTA) spectrometer equipped with a monochromatic X-ray source (Al Kα =1486.6 eV). Thermal programmed desorption coupled with mass spectrometry (TPD - MS) was used to obtain insights on the nature and the amount of oxygen-based functional groups in the bulk of the materials. Furthermore, the same technique allows the quantification of the active surface area (ASA). The analysis of TPD - MS was performed on a laboratory (IS2M) made equipment. A quantity of ~ 500 mg of HCS was heated under a secondary vacuum of 10^{-6} – 10^{-7} mmHg from 25 to 950 °C with a heating rate of 5 °C min^{-1}. The released gases were quantitatively detected and analysed using a quadrupole mass spectrometer (MS) that is already calibrated using the following reference gases, *i.e.*, H_2, H_2O, CO, and CO_2. Before each analysis, a measurement of N_2 sensibility was performed to allow further quantification of other gases[27,38,44,45]. Subsequently, the material is exposed to oxygen chemisorption at 300 °C for 10 hours, and after cooling down, a second TPD-MS is performed up to 950 °C with a heating rate of 10 °C min^{-1}. This allows quantification of the structural defects or the active surface area (ASA) of the materials. More details about this procedure can be found elsewhere[27,46].

2.3 Electrochemical Characterisation

2.3.1 Electrode preparation

The working electrodes were prepared by mixing in a ball miller (PULVERISETTE 7) at 500 rpm for 1 hour the active material (synthesised HCSs and commercial graphite), the polyvinylidene fluoride (noted PVDF from Solef 5130) binder and carbon black (Super C65 from Imerys), with a mass ratio of 90:5:5 respectively, in the presence of 1-methyl-2-pyrrolidone solvent (noted NMP (purity ≥99) from Sigma Aldrich).

The obtained slurry was coated on an aluminium current collector (20 µm thickness) using the doctor blade method (150 µm thickness), then dried under vacuum for one night at 80 °C. The electrode foil obtained was cut into round pieces using a precision punch, to obtain electrodes with a diameter of 9.5 mm and a mass load of ~ 1.4 - 1.9 mg cm^{-2}. The electrodes were dried in a Buchi oven under vacuum for one more night at the same temperature (80 °C) before being introduced into an argon-filled glove box (MBRAUN).

2.3.2 Battery testing conditions

Electrochemical analyses were performed using 2032-type coin cells in a controlled temperature room (~25 °C) with a multichannel VMP 3 system (BioLogic, France), by assembling at least two cells for each material to ensure the reproducibility of the results. The mean error was estimated to be of maximum 5%.

Coin cells were assembled using HCS and Gr-SLP30 electrodes, microporous trilayer (PP/PE/PP, Celgard) and glass microfiber filter (Whatman, Grade GF/D) as separators, and potassium metal as counter electrode. It is worth mentioning that K metal electrodes were prepared from K ingots (Alfa Aesar, 99.95%) in the following way. Teflon tweezers were used to place K metal pieces between 2 latex surfaces, followed by pressing them with the help of an 8 cm diameter Teflon roller. Then, 10 mm diameter K metal disks were punched out and the K metal disks were removed from the latex using Teflon tweezers, then placed on a stainless-steel spacer (1 mm thick, 16mm diameter) and finally scratched with the back of the tweezers, to remove oxide layer from the surface.

Most tests were performed using as electrolyte 0.8M of potassium hexafluorophosphates (KPF_6, Sigma-Aldrich, ≥99%) dissolved in a mixture of ethylene carbonate (EC, Sigma-Aldrich, ≥99%) and diethyl carbonate (DEC, Sigma-Aldrich, ≥99%) in a 50:50 v / v ratio. In addition, for the most promising material, complementary tests were conducted with other electrolytes:

0.8M of potassium bis(trifluoromethanesulfonyl) imide (KTFSI, Solvionic), 0.8M of potassium bis(fluorosulfonyl)imide (KFSI, Solvionic), 0.8M of a mixture of KPF_6 (90%) and KTFSI (10%) and 0.8M of a mixture of KPF_6 (90%) and KFSI (10%) in the same solvent mixture. Two concentrated electrolytes were also tested, which are 5M of KTFSI and KFSI in 1,2-dimethoxyethane (DME, Sigma- Aldrich).

Galvanostatic charge/discharge tests were performed between 2.0 - 0.01V (*vs.* K^+/K) in half-cells at C/20 for the first 5 cycles then at C/10 (23 mA g^{-1}) until 50 cycles. Cycling voltammetry (CV) was performed at different scan rates from 0.02-0.2 mV s^{-1} to discriminate the capacitive and diffusive behaviours of HCS materials using the Dunn method[47].

The evaluation of the rate performance was done according to several distinct protocols:

i) Conventional galvanostatic cycling test: 5 cycles at C/20 and 45 cycles at C/10 , then 5 cycles at C/10, 5 cycles at C/5, C/2, C, 2C, 5C, 10C followed by 5 cycles at C/10.

ii) First (1^{st}) alternative test: 5 cycles at different C-rates, *i.e.,* C/10, C/5, C/2, C, 2C, 5C, 10C with potassiation (insertion) kept at C/10 between C/5 to 10C (to reduce the impact of the K metal stripping polarization) followed by 5 cycles at C/10 to verify the capacity.

iii) Second (2^{nd}) alternative test: 4 cycles at C/10, potassiation at C/10 followed by successive depotassiation (at xC from x= 10, 5, 1, 0.5, 0.2, 0.1, 0.05, *i.e.,* from 5C to C/10) and 2 hours relaxation steps. The aim of this test was used to evaluate only the depotassiation (extraction) rate capability.

3. Results and discussion

3.1 Morphology, Structure, Texture and Surface properties

The morphology of the materials examined by SEM (Figure 1a and Figure S1a-c) shows individual, well-marked, and uniform spherical particles. HCS has a particle size range of 2 to 10 µm with a bimodal distribution for all materials, centred at a maximum of ~ 3.6-4.7 µm and 6.6-7.7 µm, as shown in the particle size distribution of the HCS1700 inset (Figure 1a) and for all materials (Figure 1b). The uniformity of the particles along with the size obtained are important parameters to optimize the electrode and achieve high performance in NIBs[27]. On the other hand, Gr-SLP30 presents a flakes-like morphology, with rounded particle contours (Figure S1c) and an average particle size of 32 µm[38].

The material structure was analysed by complementary techniques, *i.e.*, HRTEM, XRD, and RAMAN. As shown by HRTEM (Figure 1c) HCS1700 reveals a structure that combines a mixture of disordered graphene domains randomly orientated and *pseudo*-graphitic domains, where short graphenes (3-6 nm) are staked in 3-5 layers. Such a structure is typical for hard carbon materials[12]. The same structure is observed for the other HCS, as illustrated by the images provided in Figure S1d-e. The presence of closed pores (empty spherical spaces surrounded by few staked parallel graphene layers) can also be observed, as indicated by the yellow arrows in (Figures 1c and S1d). On the contrary, the graphite Gr-SLP30 shows a highly ordered structure with several parallel stacked of graphene (up to 25 layers), which have a long lateral size (15-30 nm) and no closed pores, as shown in Figure S1f. .

As illustrated in Figure 1d, the XRD patterns of all the HCS samples exhibit three distinct broad diffraction peaks indexed as (002) at $2\theta \approx 23°$, (100) at $2\theta \approx 44°$ and (110) at $2\theta \approx 80°$ respectively, indicating the formation of a disordered-like carbon structure. In particular, the diffraction planes (002) reveal a small shift to higher 2 theta angles and an increase in the intensity with the increase of the pyrolysis temperature (from 1500 to 1900 °C), suggesting an improvement in the structural organisation of the material. A decrease of the interplanar distance, d_{002} from 3.69 Å to 3.59 Å is observed, in agreement with other works[27,48,49]. However, d_{002} remains greater than that of Gr-SLP30 (3.35 Å). The larger interlayer distance of HCSs might manage the volume change associated with K-ion insertion/extraction[12]. For the graphite material (Figure S2a), an intense and narrow peak at 26°, specific to the (002) diffraction plane, indicates a very organized structure corresponding to hexagonal graphite (COD 9011577). Other small peaks **(**inset Figure S2a) between 42° and 46° correspond to a mixture of hexagonal and rhombohedral phases[38].

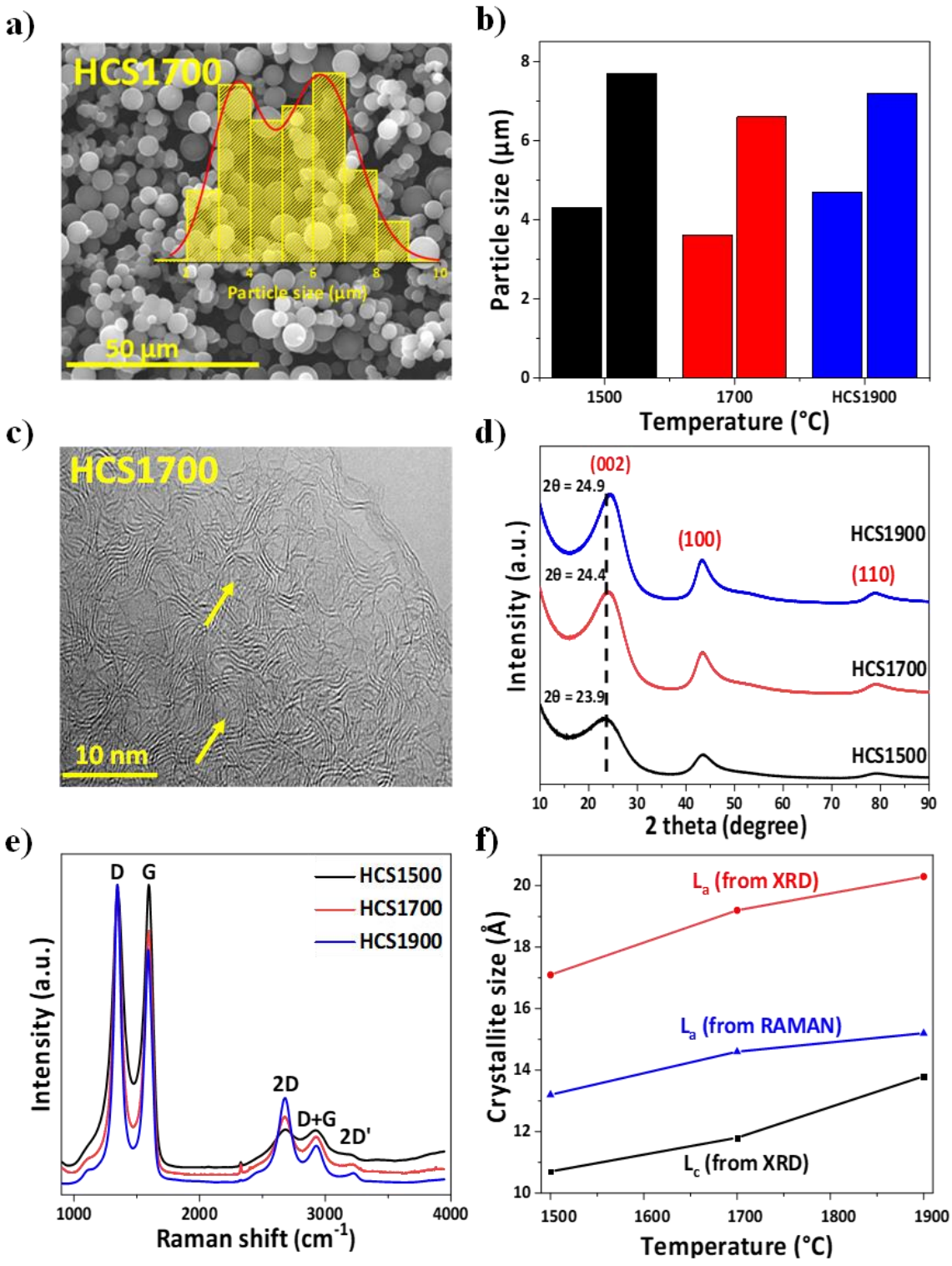

Figure 1: (a) SEM image and the particle size distribution of HCS1700 (inset); (b) Average particle size corresponding to the two peaks for HCS1500, HCS1700 and HCS1900; (c) HRTEM image of HCS1700; (d) XRD diffractograms of HCSs; (e) Raman spectra of HCSs; (f) Evolution of crystallite height (L_c) and width (L_a), calculated from XRD and Raman data, with the pyrolysis temperature.

The crystallite height (L_c) along c-axis and the crystallite width (L_a) along a-axis were calculated using Scherrer formula from the XRD data, the peaks (002) and (100), and the average number of graphene layers was also estimated as L_c/d_{002} (Table 1). Gr-SLP30 presents the highest L_c, L_a and L_c/d_{002} due to its highly organized structure. Regarding HCSs, the HCS1900 has the highest L_c and L_a values, *i.e.*, 13.8 Å and 20.3 Å, respectively, and the smallest d_{002} (3.59 Å). This confirms the increase of graphene layers stacking when increasing the pyrolysis temperature, *i.e.*, ~ 2-3 for HCS1500 and ~ 4 for HCS1900.

Table 1: Hard carbon spheres and graphite physico-chemical characteristics: particle size, graphite interlayer distance (d_{002}), crystallite height (L_c), crystallite width (L_a), number of graphene layers (L_c/d_{002}), I_D/I_G ratio, specific surface area (SSA), active surface area (ASA), oxygen (O%) and carbon (C%) surface amount, oxygen-based functional groups (CO_x) amount, He density and closed porosity ratio. *[a] determined from XRD and [b] from Raman spectroscopy*

Material properties	HCS1500	HCS1700	HCS1900	Gr-SLP30
Particle size (µm)	4.1	6.3	6.4	32
d_{002}[a] (Å)	3.69	3.64	3.59	3.35
L_c[a] (Å)	10.7	11.8	13.8	284
L_a[a] (Å)	17.1	19.2	20.3	707
L_c/d_{002}[a]	3	3	4	84
I_D/I_G[b]	1.46	1.32	1.27	0.31
N_2 SSA ($m^2\ g^{-1}$)	3.6	1.4	1.0	6.5
V_T ($cm^3\ g^{-1}$)	0.0056	0.0040	0.0030	0.0212
CO_2 SSA ($m^2\ g^{-1}$)	18	14	8	5
ASA ($m^2\ g^{-1}$)	1.6	0.1	0.1	0.4
O (at %)	5.35	1.59	1.46	3.3
C (at %)	92.4	98.2	98.2	96.7
CO_x (mmol g^{-1})	0.04	0.005	0.003	0.04
He density (g cm^{-3})	1.86	1.50	1.42	2.30

Closed porosity ratio (%)	19.6	35.1	38.6	0.8

The local structure and defects of HCS were estimated by Raman spectroscopy (Figure 1e). All materials show two intense and sharp peaks at ~ 1340 cm^{-1} and 1590 cm^{-1} corresponding to the D and G bands. The D band is related to disordered carbon, while the G band is associated with organized graphite (hexagonal carbon structure), respectively, which are typical features of carbon materials[50,51]. Both can be used to characterize the degree of graphitisation and defects by calculating the I_D/I_G ratio[19,44] . The D band has a lower intensity than the G band in organized materials, which is the case for Gr-SLP30 (Figure S2b), while the D band is more intense than the G band for HCSs, indicating a more disordered structure[52–54]. I_D/I_G ratio is calculated to be 1.46, 1.32, 1.27 (Table 1) for HCS1500, HCS1700, and HCS1900, respectively, suggesting a higher degree of graphitisation at higher pyrolysis temperature for HCSs. Gr-SLP30 shows a very low I_D/I_G ratio of 0.3 (Table 1) due to its more organized structure, which is in line with the XRD and HRTEM results. At higher Raman shift (2500-3500 cm^{-1}), other peaks with lower intensity were detected (Figure 1e and Figure S2b) and associated with 2D, D+G, 2D'. The 2D band is characteristic for bulk graphite and gives information about the degree of graphitisation in the material. The D+G band was reported as a defect activated peak and the 2D' band is the harmonic of Raman inactive fundamental mode in ordered carbons[50,51]. The intensity of this band in HCSs increases with increasing the pyrolysis temperature, confirming the formation of graphitic domains at high temperature in addition to the disordered ones[54,55]. This band is very intense in the case of graphite, Gr-SLP30.

The evolution of the crystallite width (L_a) calculated from Raman spectra for HCS (Figure 1f) shows the same trend with the pyrolysis temperature (13.2, 14.6, and 15.2 Å for HCS1500, HCS1700 and HCS1900, respectively) as (L_a) deduced by XRD results, although some differences in the values are observed, and related to the specificity of each technique.

The textural properties of the materials were determined by N_2 adsorption-desorption and CO_2 adsorption. The obtained N_2 isotherms (Figure 2a) for HCS are type II characterised by low porosity or nonporous materials and a mixture of type II/IV for Gr-SLP30 (Figure S3a) with small hysteresis starting around $P/P_0 = 0.40$ indicating capillary condensation of the mesopores. Furthermore, we can observe a significant increase in adsorbed volume at high relative pressure due to the contribution of intergranular porosity[38]. All samples have a very low BET specific surface area < 10 $m^2\ g^{-1}$ as reported in Table 1, which is favourable for potassium ion storage

because it can limit electrolyte decomposition and excessive SEI formation[56]. From the published works in the literature (Table S1)**,** it can be seen that a small SSA limits irreversible capacity.

Based on the N_2 adsorption results, the pore size distribution of HCS and Gr-SLP30 was determined (Figure 2b and Figure S3b). Two regions of porosity were revealed for HCSs, first the micropores with a pore diameter < 2 nm with a small presence of mesopores at ~3 nm, second at (~ 20-30 nm) which can be associated to inter-grains porosity. Gr-SLP30 presents the same trend as HCS in terms of porosity with micropores < 2 nm, small mesopores (~ 2.5 to 7.5 nm) and an important contribution of inter-grain porosity.

To better understand the texture of HCS, CO_2 adsorption was performed since this gas allows greater diffusion, accessibility, and rapid kinetics in narrower pores (< 0.7 nm)[44]. The CO_2 adsorption isotherm (Figure S4a) shows a slightly higher adsorbed volume than N_2 and BET surface area (Table 1), but the values are still very low (< 10 m^2 g^{-1}) and decrease with increasing pyrolysis temperature. This reveals the presence of some ultra-micropores (pores below 1.0 nm) as shown in the pore size distribution (Figure S4b). It can be assumed that this kind of porosity can have an impact in K-ion storage, as already shown in NIBs[27], however, this impact is not yet elucidated for KIBs and a limited effect is expected herein due to the low values of CO_2 SSA.

The He-density of the materials was measured (Figure 2c and Table 1) and the values are 1.86, 1.50 and 1.42 g cm^{-3} for HCS1500, HCS1700 and HCS1900, respectively, while the helium density of Gr-SLP30 is much higher*, i.e.*, 2.3 g cm^{-3}. If the electrode density is calculated according to the protocol provided in SI, the same trend was observed as for He density, *i.e.,* decreases of electrode density by increasing the pyrolysis temperature for the HCS materials, e.g. 0.82, 0,63, 0.62 g cm^{-3} for HCS1500, HCS1700 and HCS1900, respectively. On the other hand, Gr-SLP30 presents an electrode density of 0.88 g cm^{-3}. The decrease in HCS He and electrode densities by enhancing the pyrolysis temperature might be explained by the formation of a closed porosity. Therefore, the closed- and open-porosity ratios of HCS were calculated using the helium density values and the total pore volume obtained by nitrogen adsorption. As noted, (Figure 2d and Table 1), closed porosity increases from 19.6% for HCS1500 to 38.6% for HCS1900.Gr-SLP30 has a closed porosity ratio of 0.8% which is very low compared to HCS. However, open porosity decreases as the pyrolysis temperature increases for HCSs and is the lowest for Gr-SLP30 (~5 %). These differences between HCS and Gr-SLP30 are due to the type of carbon precursor and the preparation conditions, such as the temperature of

pyrolysis. Furthermore, the impact of closed porosity in K-ion storage is rarely discussed in the literature. This is noted in the different published articles in the literature, such as the ones reported in Table S1.

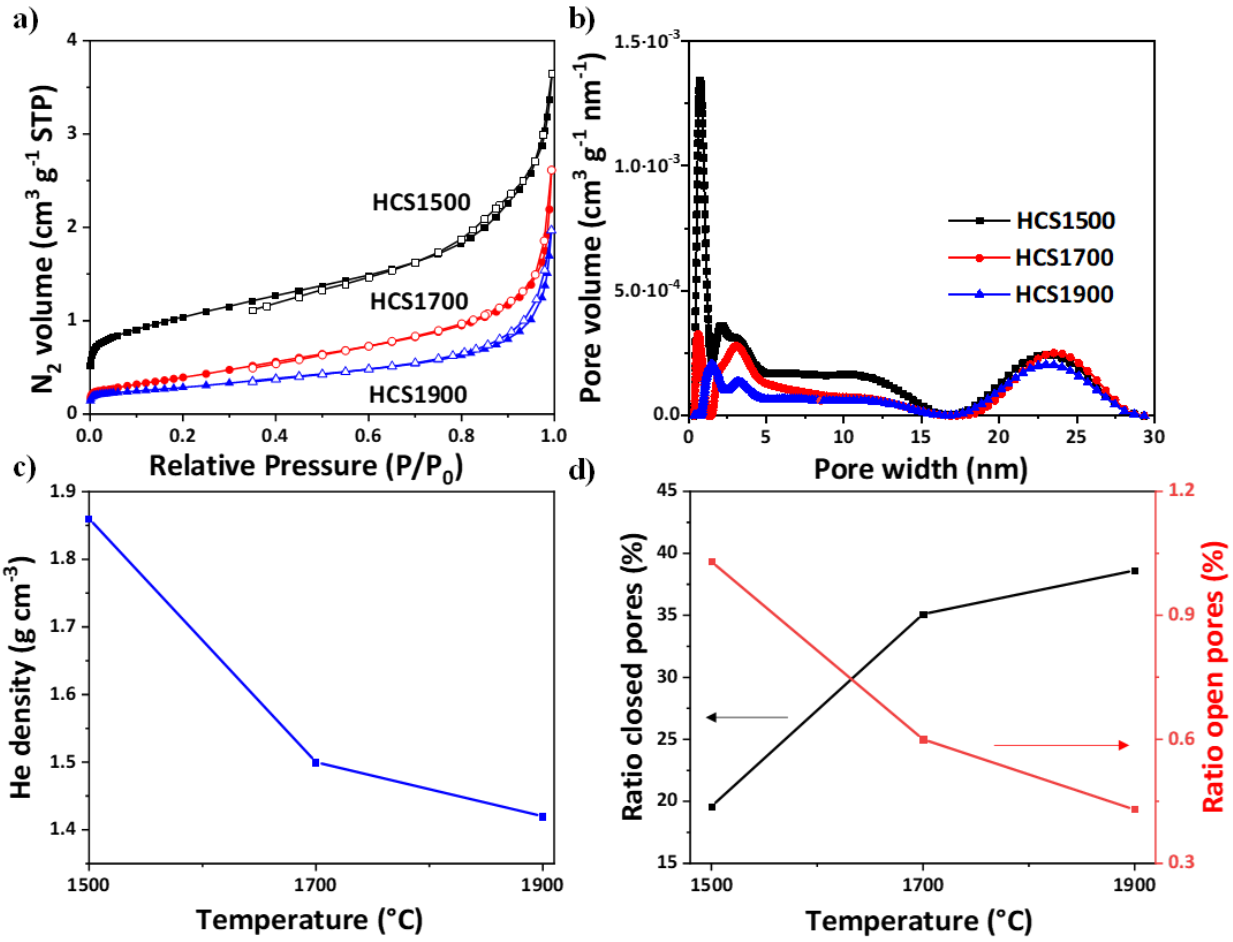

Figure 2: (a) N_2 adsorption - desorption isotherms of HCS materials; (b) pore size distribution determined using N_2 adsorption branch and the two-dimension non-local density functional theory (2D-NLDFT) model; (c) Helium density evolution with pyrolysis temperature; (d) Closed and open porosity ratio evolution with pyrolysis temperature.

X-ray photoelectron spectra (XPS) on HCSs were recorded to provide a view of the surface chemistry of the materials, namely, the nature of the functional groups and the binding energy on the surface of the material (10-15 nm) compared to the TPD-MS analysis which provides information on bulk.

The high-resolution C1 XPS spectra of the HCS materials are recorded and an intense peak corresponding to C sp^2 is observed, which increases with increasing pyrolysis temperature

(Figure 3a). In addition, other small peaks were detected as shown for HCS1500 in the high resolution deconvoluted spectra of C*1s* (Figure 3b). The peaks can be associated with C sp^3 and oxygen-based functional groups (*i.e.*, carbonyl, CO, ethers, COR, and carboxyl COOR)[45]. Some small peaks of K $2p_{1/2}$ and K $2p_{3/2}$ are only observed for HCS1500 and are associated with some contamination impurities. As shown in Figure 3c and Table 1, the amount of oxygen detected by XPS decreases (from 5.3 to 1.5 at%) by increasing the temperature of the pyrolysis. This can be beneficial for K-ion storage because it can limit electrolyte decomposition, causing SEI formation, and has high irreversible capacity in the first cycle. However, a small amount of oxygen can ensure good wettability of the carbon material by the electrolyte. On the other hand, the amount of carbon is increased (from 92.4 to 98.2 at%) with the pyrolysis temperature. This might help to have more insertion sites for a larger number of K^+. Regarding Gr-SLP30, an intense peak of C sp^2 is observed (Figure S5a) confirming the high structural order. Additionally, oxygen groups such as C=O, C-OR and O=C-O can be seen as well (Figure S5a').

Figure S6a-d shows the TPD-MS profiles of the desorbed gases during the heating under vacuum for the different samples. The oxygen-based functional groups were decomposed into CO and CO_2 groups. The latter were attributed according to their decomposition temperature to specific functional groups, as described in the literature[45,57]. For HCS and Gr-SLP30 materials, the desorption profiles show peaks of CO_2 desorption between 200 and 700 °C indicating the decomposition of carboxylic acids at low temperature, followed by lactones and anhydrides, at much higher temperature. The CO desorption exhibits peaks in the range of 300 to 900 °C resulting from the degradation of ethers, phenols, and quinones. The total amount of CO_2 and CO released (namely CO_x, Figure 3d, and Table 1) decreases for HCS with increasing temperature.

For the graphite material, the CO and CO_2 profiles have intensities higher than those of the HCS materials. As a consequence, the total amount of COx is more than ten times higher for graphite than HCS1900, but similar to that of HCS1500. However, the values are very low compared to reported data for other HCs and graphites[27,38]. Other gases were also desorbed such as H_2 (~600 °C) due to the C-H bond cleavage, in greater quantities for HCS series, indicated more disorganized materials. Water is also released (50 to 600 °C)[45] due to physisorption into the pores and/or secondary reactions occurring between neighbouring oxygen-functional groups (-COOH, -OH, etc.).

Both of the TPD-MS and XPS techniques showed the presence of oxygen based functional groups in the HCSs which decrease as the pyrolysis temperature increases.

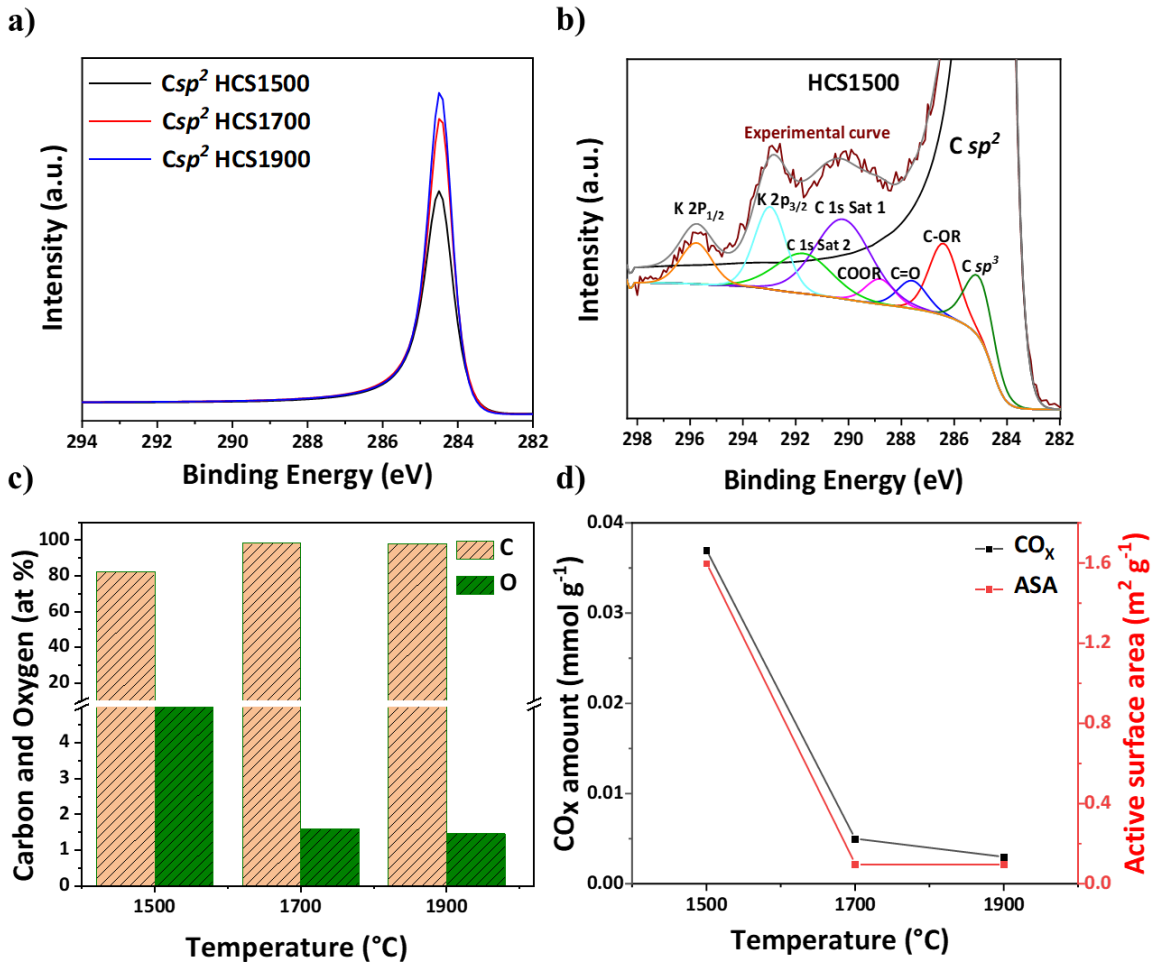

Figure 3: (a) XPS C sp^2 high-resolution peak of the HCSs; (b) XPS C1s high-resolution deconvoluted spectra of HCS1500; (c) carbon and oxygen amount evolution with pyrolysis temperature as determined by XPS; (d) the amount of oxygen-based functional groups (CO_x) and the active surface area (ASA) *vs.* pyrolysis temperature assessed by TPD-MS.

Surface defects can be involved in the storage mechanism of K ions and irreversible capacity, similar to Na and Li ions, as shown with both hard carbons and graphite[27,38,58]. Therefore, a quantification of the edge defects and active sites was carried out by measuring the active surface area (ASA) after the surfaces of the materials were cleaned during the first TPD-MS analysis. Figure 3d shows the evolution of the active surface ASA *vs.* pyrolysis temperature for HCS. Very low ASA values were obtained for HCS and decreased from 1.6 $m^2\ g^{-1}$ for HCS1500 to ~ 0.1 $m^2\ g^{-1}$ for HCS1700 and HCS1900. The latter have four times lower ASA values (0.1 $m^2 g^{-1}$) than Gr-SLP30 (0.4 $m^2\ g^{-1}$). Moreover, ASA quantification is absent in the literature for carbons used in KIBs, contrary to that for NIBs. For example, this property was not mentioned in the published works presented in Table S1.

3.2 Electrochemical properties

The performance of HCS and Gr-SLP30 materials as negative electrodes in KIBs, in terms of CE, capacity retention, and rate performance, were determined and further correlated to the carbon properties (structure, texture, and chemistry).

Figures 4a-b depict the galvanostatic charge/discharge profiles for HCS1500, HCS1700, HCS1900, and Gr-SLP30 electrodes during the 1st cycle at C/20 and 50th cycle at C/10 rate.

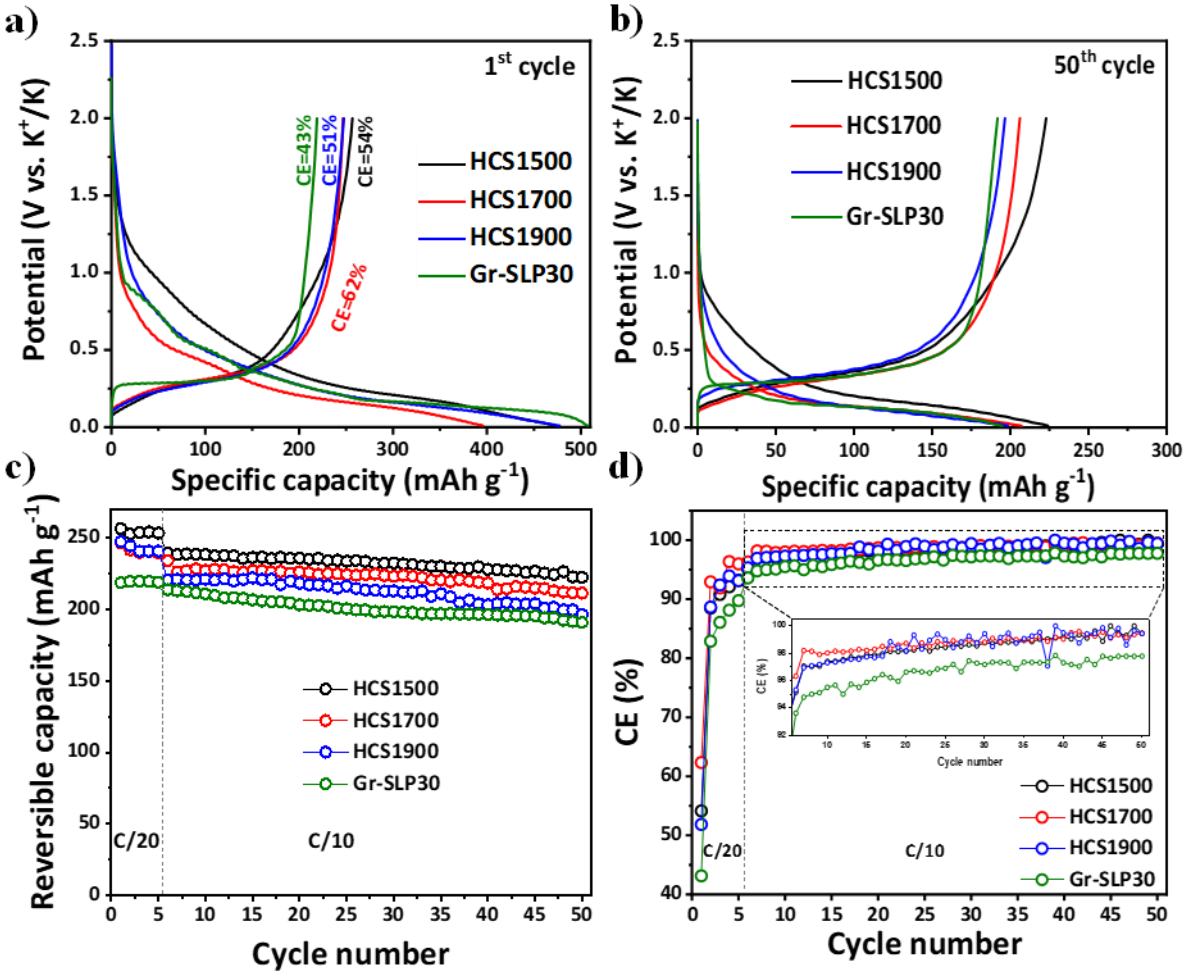

Figure 4: Galvanostatic profiles of the (a) 1st and (b) 50th cycle at C/20 and C/10, respectively; (c) capacity retention; (d) Coulombic efficiency at C/10 rate after 5 formation cycles at C/20 obtained between 2.0-0.01 V for HCS1500, HCS1700, HCS1900, and Gr-SLP30 electrodes.

The shape of the curves presents two distinct regions: a sloping region from 2.0 to 0.35V and a plateau-like region from 0.35 to 0.01 V. When we compare the first plateau region between HCS materials (Figure 4a), we noticed that the lengths are longer for HCS1700, HCS1900, and Gr-SLP30 compared to HCS1500, which presents a higher slope region (*i.e.*, capacitive behavior). After 50 cycles (Figure 4b), the slope region becomes less pronounced for all

materials. Therefore, a considerable decrease in irreversible capacity is remarked along with a decrease in reversible capacity.

The high irreversible capacity is essentially attributed to the formation of SEI involving the reduction of the electrolyte on the electrode surface and the trapping of K^+ in porosity or/and structure[59,60]. Although there is not yet a complete agreement on the association of these regions with a precise mechanism, several works [61–63] suggest that K-ions are adsorbed to defective sites or pores in the sloping region, while insertion of K ions between graphene layers or filling in closed pores occurs in the plateau region.

In addition, the arrangement of the graphene layers might affect the adsorption / diffusion phenomena. Graphite presents a highly organized structure and small inter-planner distances (3.35 Å) and the K-ion diffusion through the planes can be unidimensional, while the hard carbon materials present a disordered structure with randomly orientated planes and higher interlayer distances (3.59 to 3.69 Å). Therefore, the diffusion of K-ion is multidimensional (in different directions) and easier to occur. Figure 4c shows the capacity retention over 50 cycles. HCS1500 has 88% capacity retention compared to 83%, 79%, and 87% for HCS1700, HCS 1900, and Gr-SLP30, respectively (Table 2). In terms of CE evolution (Figure 4d), for HCS1700, it reaches 98% after 10 cycles, while CE for HCS1500 and HCS1900 reaches 98% after 18 cycles. Concerning Gr-SLP30, it does not reach 98% even after 50 cycles. High retention is maintained for all materials after 50 cycles (Table 2). Based on these results, HCS1500 shows the best tradeoff based on reversible capacity, capacity retention, and CE evolution. It is important to mention that other factors that are not related to the electrodes contribute as well to the low ICE observed. For example, it was shown that the reactivity of K-metal might induce electrolyte degradation and SEI formation[64]. The electrolyte itself, in particular, the anion, plays an important role in the formation of SEI. As will be explained later in the manuscript (Figure 8 a-b), better ICE is obtained when KTFSI and KFSI electrolytes are used compared to KPF_6 in EC: DEC.

To gain insight into the mechanisms that occur in these materials, CV analyses were performed (Figure S7). A similar CV profiles for HCS1500, HCS1700, and HCS1900 with two redox peaks (O_1/R_1) reflecting the insertion/extraction of K ions (diffusive behavior) is seen. For a given scan rate, the hysteresis between the 2 redox peaks (anodic and cathodic pics) increases as the pyrolysis temperature. This suggests a decrease in polarization, and a rate capability improvement. By enhancing the scan rate, the peaks become more intense, no matter the material, indicating that capacitive phenomena are promoted. If the capacitive (adsorption) and

diffusive (insertion) contributions are determined based on CV curves and Dunn method, the increase of capacitive phenomena can be clearly seen with the scan rate to the detriment of the diffusive process (Figure 5a-b). The evolution of both capacitive and diffusive contributions between 0.02 - 0.2 mV s^{-1} scan rate CV shows that the diffusion contribution is predominant (~70 to 90%) compared to the capacitive one (~10 to 30%). HCS1500 and HCS1900 have similar behaviour, while HCS1700 show more pronounced diffusive behaviour. Furthermore, the capacitive contribution depicted in Figure 5a is sustained by the capacitive contribution (slope zone in the galvanostatic curves) which is larger for HCS1500 and HCS1900 compared to a tiny slope region for HCS1700 (Figure 4a).

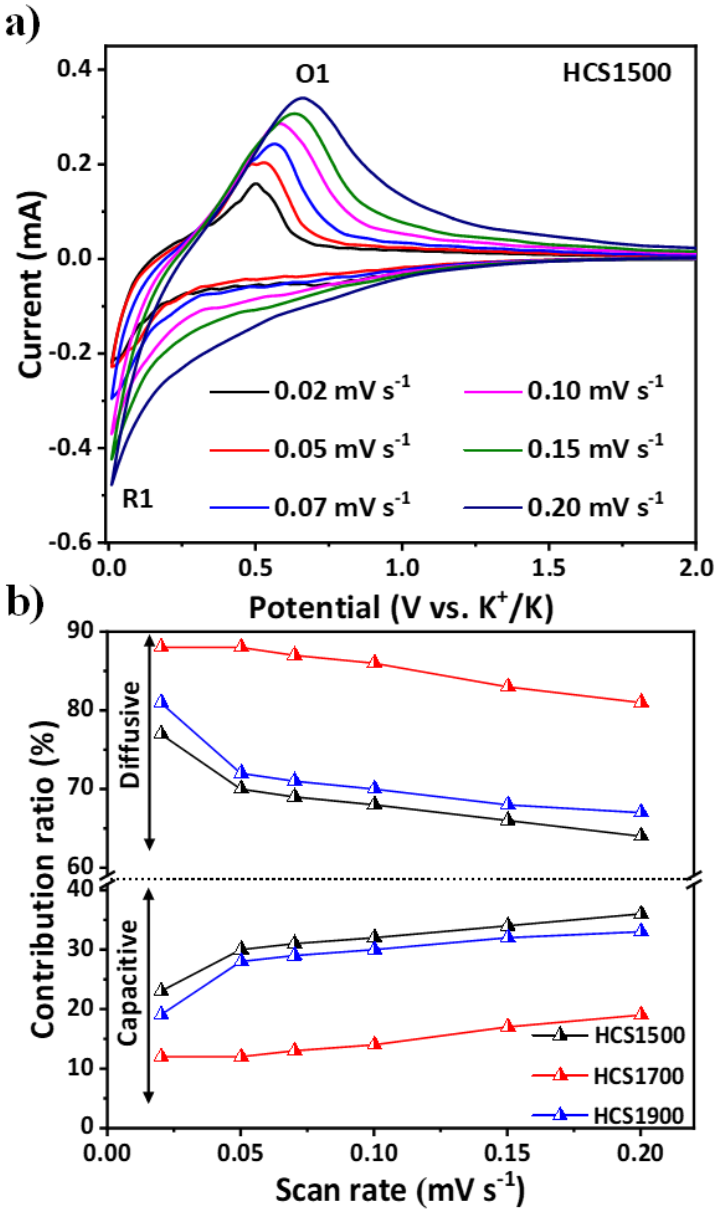

Figure 5: (a) Cyclic voltammetry at different scan rates for HCS1500; (b) Diffusive and capacitive contribution at different scan rates of HCS1500, HCS1700, and HCS1900.

Moreover, the low ICE in the whole series can also be explained by the PVDF strong swelling characteristics[65].

Regarding capacity, HCS1500 has the best initial charge capacity of 254 mAh g^{-1}, followed by HCS1700 (247 mAh g^{-1}) and HCS1900 (247 mAh g^{-1}), while graphite material delivers the lowest capacity, *i.e.*, 219 mAh g^{-1}. It seems that the obtained values decrease with increasing pyrolysis temperature. It is worth to remind that various properties such as interlayer space, open porosity, and defects are decreasing with the temperature while the closed porosity shows an opposite trend. These properties are known to affect the insertion/adsorption sites of K^+ ions[22]. If we attempt to correlate the first charge capacity with the interlayer space, d_{002}, (Figure 6a-b**)**, we can see that the capacity increases with the expansion of d_{002} and, therefore, with the decrease of the pyrolysis temperature. This is in agreement with other works[48,49], and is emphasized in Table S1. For example, Kubota *et al.*[66] showed that when the pyrolysis temperature is increased from 1300 to 2000 °C, the reversible capacity decreases. Therefore, larger interlayer spaces allow for better accommodation of K^+ considering their size, which is larger than that of Li^+.

Defects are also claimed to play a role in K-ion adsorption. As seen in Figure 6a,c, the capacity is enhanced with increasing defect ratio (I_D/I_G). The important role of defects in the insertion capacity has already been observed in hard carbon used in KIBs and NIBs [40].

Concerning the possible impact of closed pores on the capacity, one can see **(**Figure 6a,d**)** within the HCS series that the capacity tends to increase (HCS1500) with the decrease of the porosity. In the case of graphite, which has much lower closed porosity, the capacity is reduced. These results suggest that closed porosity does not contribute to K-ion storage. The mechanisms suggesting the closed pore contribution in Na-ion storage have been widely debated in NIBs [67,68] and are still controversial in the K-ion counterpart.

HCS1700 has the highest ICE (62%) followed by that of HCS1500 (54%) and finally HCS1900 (51%) and Gr-SLP30 (43%), respectively. The higher ICE of HCS1700 can be related to its low SSA, low ASA, and optimal d_{002} compared to its analogues prepared at 1500 and 1900 °C. Indeed, HCS1500 presents much higher SSA, ASA, and CO_x functional groups that could favor SEI formation. For HCS1900, although it presents SSA and ASA similar to HCS1700, it has smaller d_{002} that can lead to irreversible trapping of K ions and thus to a lower ICE. Gr-SLP30 has the lowest initial ICE of 43% which can be attributed to its higher active surface areaand oxygen functionality amount, which could contribute to higher electrolyte degradation and thus

more abundant SEI formation[34]. In addition, ICE appears to be higher when the closed porosity is higher except for HCS1900, However, the variation of other parameters is simultaneously occurring when the pyrolysis temperature increases (SSA, ASA, CO_x %), therefore, it is difficult to distinguish the real impact of the closed porosity on ICE in this case. Furthermore, the smallest interlayer space of HCS1700 and Gr-SLP30 (3.35 Å) can irreversibly trap K-ions and likely contribute to the lower ICE[34].

Therefore, the trend of ICE evolution with temperature is not clear because of the contribution of several parameters. The same conclusion can be reached by analyzing several data from the literature collected in Table S1, which show no clear correlation of ICE with the physico-chemical properties. Nevertheless, the ICE values obtained in this work are among the best reported in the literature (Table S1), when using a similar electrode formulation (based on PVDF binder). In addition, the use of only 5% of binder is another advantage of the electrodes reported herein.

To further discriminate the impact of disordered carbon materials (HCS) and well-ordered carbon material (Gr-SLP30), the C- rate performance was evaluated after 50 cycles (Figure S8). All carbons show dramatic loss of capacity when the rate is increased. HCS1500 withstands better at high C rates, although its capacity decreased from ~235 mAh g^{-1} at C/10 rate to ~125 mAh g^{-1} at C/2 (115 mA g^{-1}) rate. This is comparable to SLP50[69] (Table S1) which delivers a capacity of 100 mAh g^{-1} at 140 mA g^{-1} after 50 cycles.

The current limit beyond which the delivered capacity is zero is 2C, C/2 and C/5 for HCS1500, HCS1700, and HCS1900 respectively. The improved results for HCS1500 is explained by the larger d_{002} that can contribute to the faster insertion/disinsertion of K-ions and more efficient rate capability. The oxygen-functional groups, porosity and defects might also favor the K ion adsorption on this material, particularly at high rates, where the capacitive behaviour is enhanced. Indeed, Kubota *et al.*[66] suggested that the presence of hydrogen terminated edges at low pyrolysis temperature (1300 °C) will allow a better adsorption compared to higher temperature pyrolysis (*i.e.*, 1800 or 2000 °C). At C/2, Gr-SLP30 delivered a lower capacity than HCS1500, but a larger capacity than HCS1700 and HCS1900. Active surface area and oxygen-based groups are higher for Gr-SLP30, which might positively contribute to a capacity increase through adsorption.

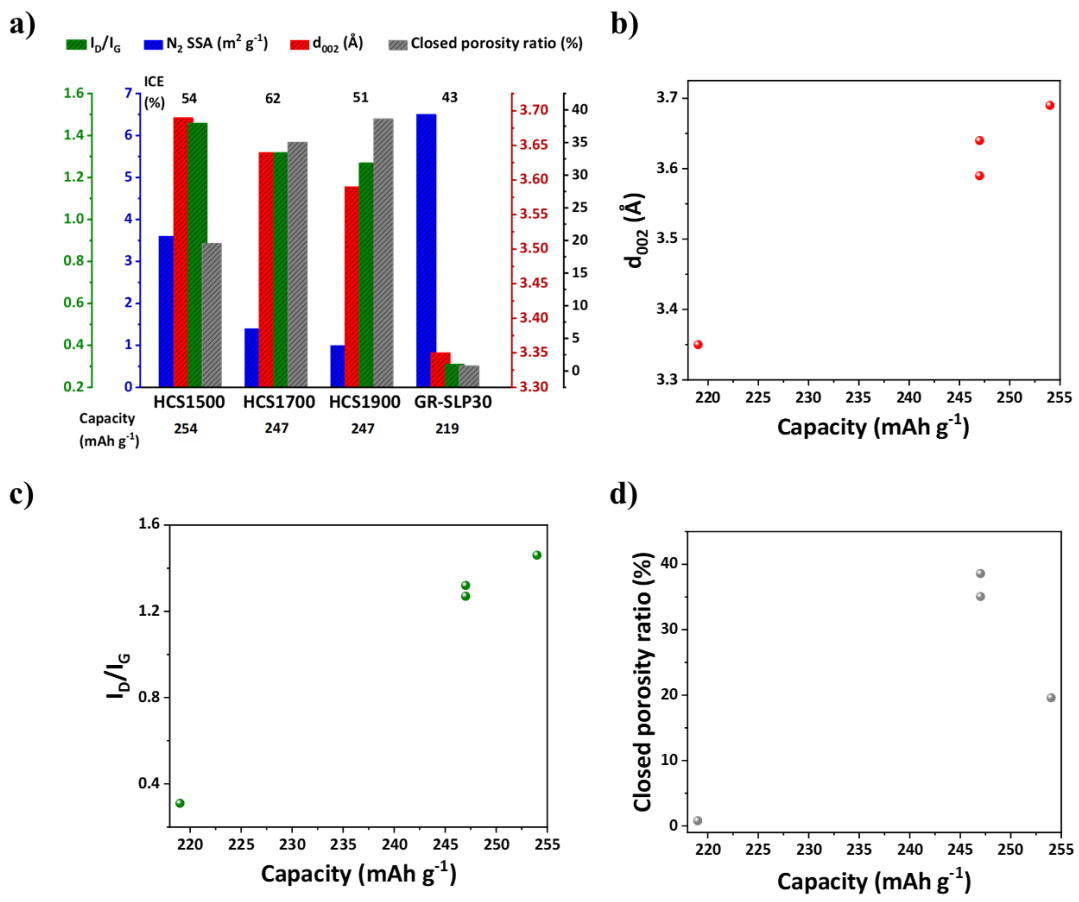

Figure 6: (a) Correlation between the N_2 specific surface area, d_{002}, I_D/I_G, closed porosity ratio and electrochemical performance (initial Coulombic efficiency and first charge capacity); (b), (c) and (d) correlation between d_{002}, I_D/I_G, closed porosity ratio and the first charge capacity.

Table 2: Electrochemical characteristics of HCSs and Gr-SLP30 including ICE, the first charge capacity, and the capacity retention after 50 cycles, respectively.

Materials	ICE (%)	1st charge capacity (mAh g^{-1})	Capacity after 50 cycles (mAh g^{-1})	Capacity retention after 50 cycles (%)	CE after 50 cycles
HCS1500	54	254	221	88	99
HCS1700	62	247	205	83	99
HCS1900	51	247	195	79	98
Gr-SLP30	43	219	190	87	97

In addition, K metal passivation upon cycling (*i.e.*, K metal stripping polarization increase) is also at the origin of the capacity decay observed during the conventional rate test in half cell[70]. As a result, the potassiation rate is restricted by the polarization of the potassium metal stripping.

To tackle this issue, two alternative cycling tests were performed at different rates. In the first alternative test, (Figure 7a**)**, the potassiation rate was kept at C/10, while the depotassiation rate varied from C/10 to 10C. Compared to the conventional rate test, substantially higher depotassiation capacities were obtained. Using this rate capability test (Figure 7a), HCS1500 delivered 230 mAh g^{-1} after depotassiation at 10C, compared to 0 mAh g^{-1} using the conventional test (Figure S8). These results show that HCS materials can give high capacities at a high depotassiation rates when the hard carbon potassiation is not limited by the K metal stripping polarization. After cycle 32 at 10 C in depotassiation (Figure 7a**)**, HCS deliver high capacities of 230, 228, and 214 mAh g^{-1} for HCS1500, HCS1700, and HCS1900, respectively, compared to 147 mAh g^{-1} for Gr-SLP30.

These high capacities for HCSare associated with a small potential hysteresis (polarization) in the 32nd cycle, especially at a high depotassiation rate (10C) when the potassiation of HCS (C/10) is not limited by the stripping polarization of K metal (Figure 7b). Furthermore, when the current goes back to lower values (C/10) after 35 cycles, HCS recover nearly all their initial capacities, but Gr-SLP30 only recovers 83% of its first capacity (Figure 7a). Moreover, this large difference in capacities between graphite and HCSs may be explained by the lower polarization of the latter compared to the high polarization of graphite, which exceeds 0.8V at 10C. The large volume changes of graphite applying extra stress on the binder and protective SEI explains the graphite behavior as well.

A second rapid alternative test (see the experimental section) was performed to evaluate only the capability of the depotassiation rate, overcoming potassium ageing and reactivity (Figure S9). In general, much higher depotassiation capacities were obtained compared to the conventional rate test mentioned above (Figure S8). For instance, the HCS1500 delivered 245 mAh g^{-1} during depotassiation at 10C (254 mAh g^{-1} at C/10) using the rapid alternative test, compared to 202, 214, 195 for HCS1700, HCS1900, and Gr-SLP30, respectively at 10C depotassiation rate. These results also confirm that HCS1500 delivers high capacities due to the large interlayer space, and higher amount of defects. This offers easy potassium adsorption/insertion without significant structural damage.

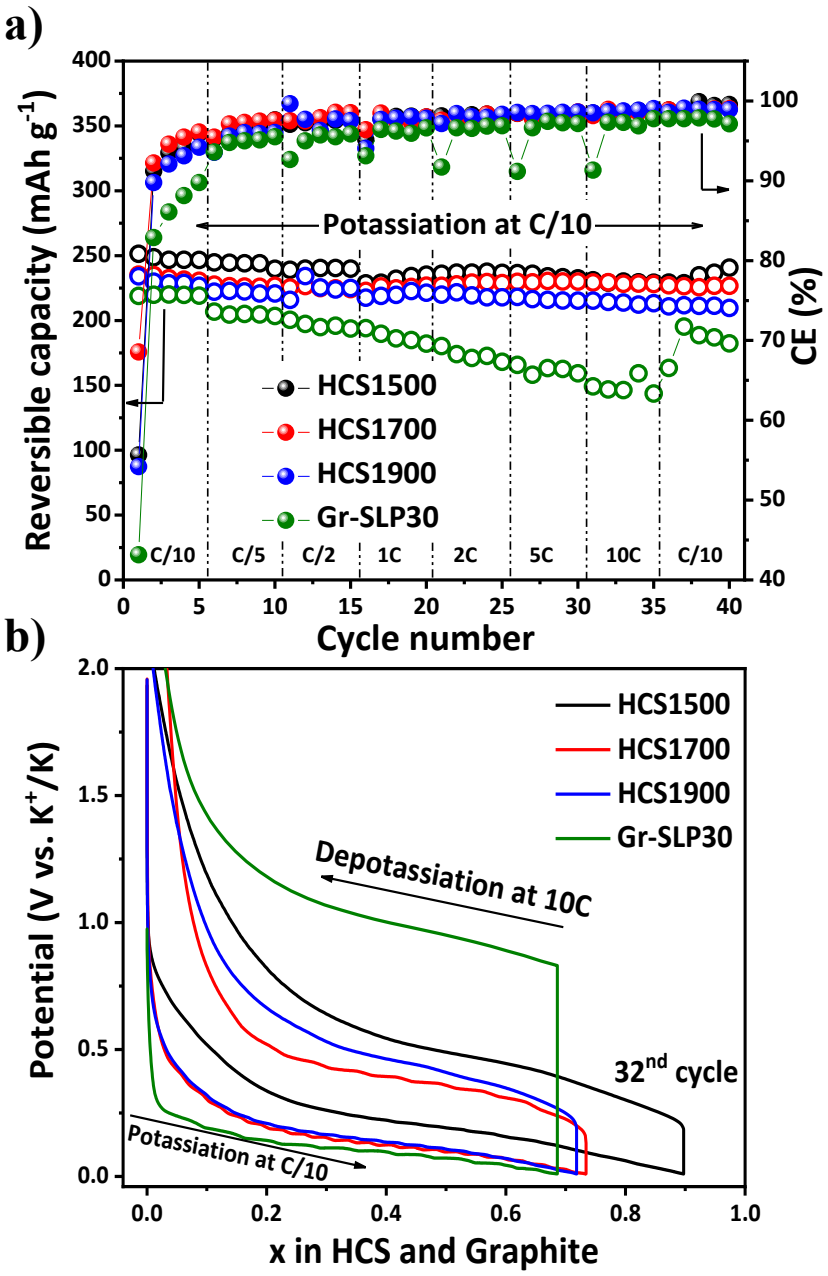

Figure 7: (a) First alternative galvanostatic rate performance from C/10 to 10C depotassiation and C/10 potassiation and CE evolution; (b) Galvanostatic profiles of the 32nd cycle at C/10 potassiation and 10C depotassiation obtained between 2.0-0.01 V for HCS1500, HCS1700, HCS1900, and Gr-SLP30 electrodes.

The material showing the best ICE (HCS1700) (was tested using different electrolytes at C/10 in half-cells *vs.* K-metal: i. using non-concentrated electrolytes 0.8M of (KPF_6, KFSI, KTFSI), ii) a mixture of 0.8M (0.9 KPF_6 and 0.1 KTFSI) and a mixture of 0.8M (0.9 KPF_6 and 0.1KFSI) both in EC/DEC and iii) two concentrated electrolytes *i.e.*, 5M KTFSI and 5M KFSI in DME, respectively. The corresponding galvanostatic charge/discharge curves are shown in Figure 8a, and two regions are observed, a slope and a plateau region for all the electrolytes, with two pronounced peaks at ~1V for 5M KFSI and 0.8V for 5M KTFSI, associated with SEI formation. The 0.8M KTFSI electrolyte exhibits a higher ICE (72%) than the 0.8M KPF_6 electrolyte (62%), but a lower first charge capacity of 187 mAh g^{-1} (0.8M KTFSI) *vs* 247 mAh g^{-1} for 0.8M KPF_6. A good compromise is observed for the 0.8M KFSI electrolyte, which showed an improved ICE (67%) with a similar 1st charge capacity (247 mAh g^{-1}) compared to the 0.8M KPF_6 electrolyte used in this preliminary study.

In addition, when using highly concentrated electrolytes (5M KTFSI in DME and 5M KFSI in DME), it is noticed that the same ICE (62%) with 0.8M KPF_6 is obtained, while both of them have a lower capacity of 213 mAh g^{-1} *vs.* 247 mAh g^{-1}. Furthermore, the mixture of 0.8M (0.9 KPF_6 + 0.1 KFSI) and 0.8 M (0.9 KPF_6+ 0.1 KTFSI) delivers ICEs of 59% and 67% and capacities of 232 mAh g^{-1} and 207 mAh g^{-1}.

The evolution of specific capacity and Coulombic efficiency during 12 cycles for HCS1700 using the different electrolytes are shown in Figure S10 a-b. It was noticed that 0.8M KFSI and 0.8M KPF_6 in EC:DEC electrolytes deliver the best cycling stabilities (capacity retention). 0.8M KPF_6 shows better cycling stability until the 6th cycle, while 0.8M KFSI behaves better for the rest of cycles. Regarding the impact on the Coulombic efficiency, all electrolytes lead to improved values compared to 0.8M KPF_6, except 0.8M (0.9 KPF_6+0.1KTFSI) in EC:DEC. Finally, 0.8M KFSI in EC:DEC seems to present the best compromise (capacity /Coulombic efficiency) during cycling. Although, long-term cycling and rate performance tests should be performed to select the best electrolyte, these results already highlight that improvement can be obtained by tuning the electrolyte formulation (including the use of electrolyte additives) in the future.

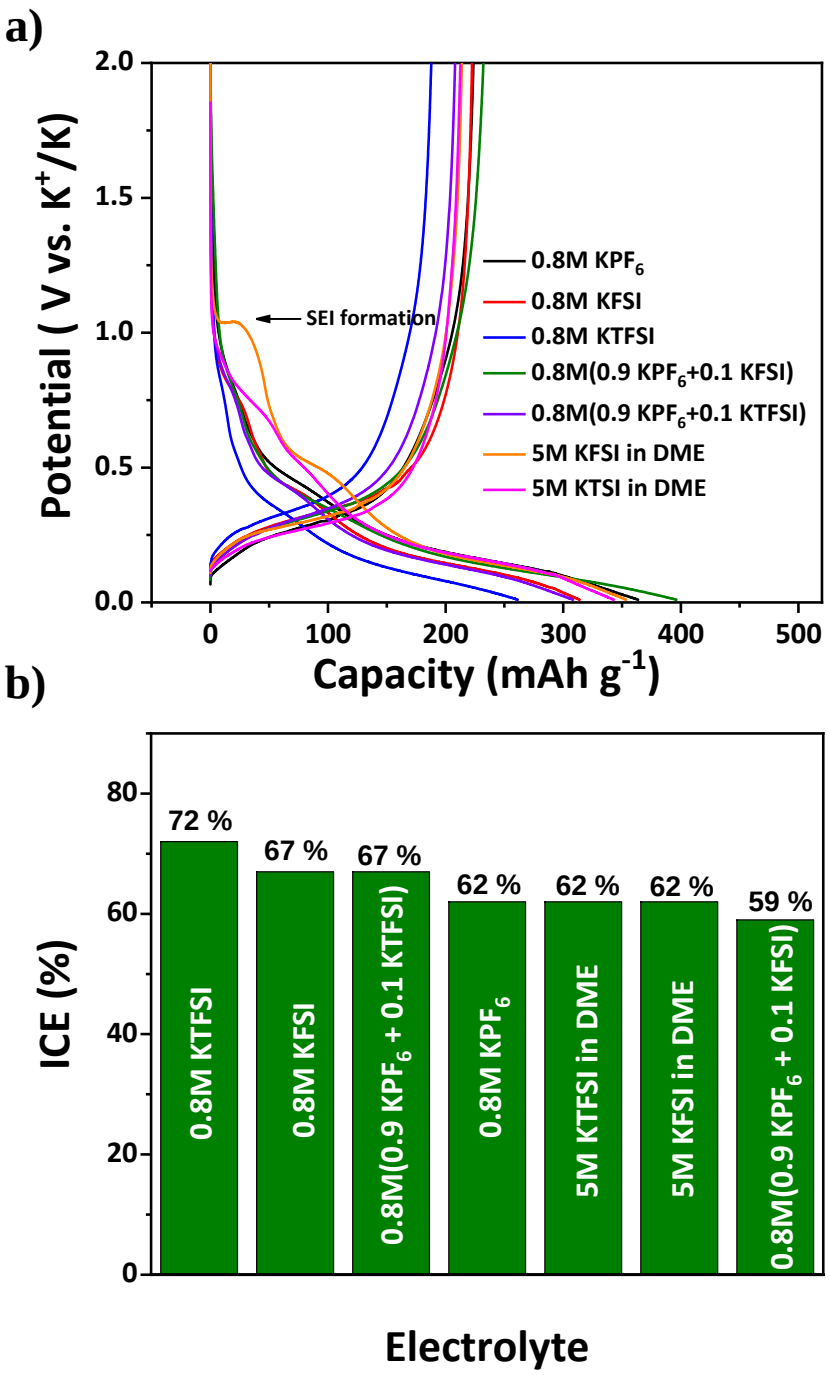

Figure 8: a) Galvanostatic 1st charge/discharge profiles and b) corresponding ICE for HCS1700 obtained between 2.0-0.01 V at C/10 using different electrolytes.

Conclusions

Hard carbon sphere (HCS) materials synthesized from a green precursor at different pyrolysis temperatures were designed to understand the influence of temperature on the physico-chemical and electrochemical properties. The results obtained were then compared to a commercial graphite (Gr-SLP30). The increasing pyrolysis temperature (1500 to 1900 °C) impacted the physicochemical properties of the HCSs. The interlayer space (d_{002}), the specific surface area, the number of oxygen-based groups and defects decreased with increasing temperature. Unlike, both helium density measurements and closed porosity have an opposite trend. Compared to HCS, Gr-SLP30 presents a different morphology (flakes *vs* spheres), lower interlayer space, no closed porosity and high density. Moreover, it reveals higher particle size, He density, and active surface area (ASA) than HCS.

The correlations between the physico-chemical properties and electrochemical performance, *i.e.,* higher capacity and capacity retention when the pyrolysis temperature is decreased, showed that the increase of the interplanar graphitic distance and defect ratio is desirable for higher performance. Regarding the ICE, the correlations were less obvious since many parameters may impact it, *i.e.*, surface chemistry, defects, and interlayer space. HCSs present better ICE and capacity compared to graphite. Furthermore, conventional C-rate tests showed rapid fading of the capacity with increasing C-rate. The alternative rate tests implemented allow to achieve high capacities (230, 228 and 214 mAh g^{-1}) at high depotassiation rates (10C) when the potassiation of the HCSs materials is not limited by the K metal polarisation. Among the materials, the HCS1500 delivers the best capacities due to its structure, which combines the larger space between the graphene layers, defects, and functionalities.

Finally, this work will contribute to the development of high-energy KIBs by providing hard carbon with suitable properties which are tuned by the synthesis conditions. Furthermore, no doubt that electrolyte formulation will allow for further improvements of the HC-based KIB, as shown here with preliminary results.

Conflict of Interest

The authors declare no conflict of interest.

Supporting Information:

SEM and HRTEM images of hard carbons and graphite; XRD and Raman spectra of graphite; CO_2 sorption isotherms and pore size distribution of hard carbon materials; XPS C1s high resolution spectra of graphite; TPD-MS gas desorption profiles of the three hard carbon and graphite material; electrode density calculation explanations; cyclic voltammetry of hard carbon materials; rate performance after 50 cycles of hard carbons; alternative rate performance test and depotassiation capacities obtained using the alternative rate performance of hard carbon and graphite materials; specific capacity and evolution of coulombic efficiency of HC1700 during cycling using different electrolytes; comparison table of physico-chemical properties and electrochemical performance of the as-prepared materials with other reported carbons in the literature.

Acknowledgements

This work was financially supported through the Algerian ministry of high education and scientific research. The authors thank financial support for electrochemical test realization through TROPIC project supported by Agence Nationale de la Recherche (ANR), Grant ANR-19-CE05-0026.

The authors thank the technical staff of "Carbon and Hybrid Material" team (Joseph Dentzer and Bénédicte Réty) for their daily support with the fabrication and analyses of carbon materials. The authors thank Dr. Loïc Vidal (HRTEM images), Dr. Jean-Marc Le Meins (XRD data) and Dr. Cyril Vaulot (gas adsorption) for technical support *via* IS2M technical platforms. The authors thank the technical staff of ICGM for their experimental help.

References

(1) Mauger, A.; Julien, C. M.; Armand, M.; Zaghib, K. Tribute to John B. Goodenough: From Magnetism to Rechargeable Batteries. *Adv. Energy Mater.* **2021**, *11* (2), 2000773. https://doi.org/10.1002/aenm.202000773.

(2) Ye, M.; Hwang, J.-Y.; Sun, Y.-K. A 4 V Class Potassium Metal Battery with Extremely Low Overpotential. *ACS Nano* **2019**, *13* (8), 9306–9314. https://doi.org/10.1021/acsnano.9b03915.

(3) Eftekhari, A. Potassium Secondary Cell Based on Prussian Blue Cathode. *J. Power Sources* **2004**, *126* (1–2), 221–228. https://doi.org/10.1016/j.jpowsour.2003.08.007.

(4) Ahmed, S. M.; Suo, G.; Wang, W. A.; Xi, K.; Iqbal, S. B. Improvement in Potassium Ion Batteries Electrodes: Recent Developments and Efficient Approaches. *J. Energy Chem.* **2021**, *62*, 307–337. https://doi.org/10.1016/j.jechem.2021.03.032.

(5) Zhang, C.; Zhao, H.; Lei, Y. Recent Research Progress of Anode Materials for Potassium-ion Batteries. *ENERGY Environ. Mater.* **2020**, *3* (2), 105–120. https://doi.org/10.1002/eem2.12059.

(6) Yan, Z.; Obrovac, M. N. Quantifying the Cost Effectiveness of Non-Aqueous Potassium-Ion Batteries. *J. Power Sources* **2020**, *464*, 228228. https://doi.org/10.1016/j.jpowsour.2020.228228.

(7) Zhao, Q.; Wang, J.; Lu, Y.; Li, Y.; Liang, G.; Chen, J. Oxocarbon Salts for Fast Rechargeable Batteries. *Angew. Chem. Int. Ed.* **2016**, *55* (40), 12528–12532. https://doi.org/10.1002/anie.201607194.

(8) Ruan, J.; Wu, X.; Wang, Y.; Zheng, S.; Sun, D.; Song, Y.; Chen, M. Nitrogen-Doped Hollow Carbon Nanospheres towards the Application of Potassium Ion Storage. *J. Mater. Chem. A* **2019**, *7* (33), 19305–19315. https://doi.org/10.1039/C9TA05205D.

(9) Caracciolo, L.; Madec, L.; Gachot, G.; Martinez, H. Impact of the Salt Anion on K Metal Reactivity in EC/DEC Studied Using GC and XPS Analysis. *ACS Appl. Mater. Interfaces*, **2021**, *13* (48), 57505-57513. ff10.1021/ascami.1c19537ff.ffhal-03516191.

(10) Madec, L.; Gabaudan, V.; Gachot, G.; Stievano, L.; Monconduit, L.; Martinez, H. Paving the Way for K-Ion Batteries: Role of Electrolyte Reactivity through the Example of Sb-Based Electrodes. *ACS Appl. Mater. Interfaces* **2018**, *10* (40), 34116–34122. https://doi.org/10.1021/acsami.8b08902.

(11) Eftekhari, A.; Jian, Z.; Ji, X. Potassium Secondary Batteries. *ACS Appl. Mater. Interfaces* **2017**, *9* (5), 4404–4419. https://doi.org/10.1021/acsami.6b07989.

(12) Lei, H.; Li, J.; Zhang, X.; Ma, L.; Ji, Z.; Wang, Z.; Pan, L.; Tan, S.; Mai, W. A Review of Hard Carbon Anode: Rational Design and Advanced Characterization in Potassium Ion Batteries. *InfoMat* **2022**, *4 (2)*, e12272. https://doi.org/10.1002/inf2.12272.

(13) McCulloch, W. D.; Ren, X.; Yu, M.; Huang, Z.; Wu, Y. Potassium-Ion Oxygen Battery Based on a High Capacity Antimony Anode. *ACS Appl. Mater. Interfaces* **2015**, *7* (47), 26158–26166. https://doi.org/10.1021/acsami.5b08037.

(14) Zuo, X.; Chang, K.; Zhao, J.; Xie, Z.; Tang, H.; Li, B.; Chang, Z. Bubble-Template-Assisted Synthesis of Hollow Fullerene-like MoS_2 Nanocages as a Lithium Ion Battery Anode Material. *J. Mater. Chem. A* **2016**, *4* (1), 51–58. https://doi.org/10.1039/C5TA06869J.

(15) Gabaudan, V.; Monconduit, L.; Stievano, L.; Berthelot, R. Snapshot on Negative Electrode Materials for Potassium-Ion Batteries. *Front. Energy Res.* **2019**, *7*, 46. https://doi.org/10.3389/fenrg.2019.00046.

(16) Ma, Z.; Cui, Y.; Xiao, X.; Deng, Y.; Song, X.; Zuo, X.; Nan, J. A Reconstructed Graphite-like Carbon Micro/Nano-Structure with Higher Capacity and Comparative Voltage Plateau of Graphite. *J. Mater. Chem. A* **2016**, *4* (29), 11462–11471. https://doi.org/10.1039/C6TA02195F.

(17) Li, J.; Li, Y.; Ma, X.; Zhang, K.; Hu, J.; Yang, C.; Liu, M. A Honeycomb-like Nitrogen-Doped Carbon as High-Performance Anode for Potassium-Ion Batteries. *Chem. Eng. J.* **2020**, *384*, 123328. https://doi.org/10.1016/j.cej.2019.123328.

(18) Wang, G.; Xiong, X.; Xie, D.; Lin, Z.; Zheng, J.; Zheng, F.; Li, Y.; Liu, Y.; Yang, C.; Liu, M. Chemically Activated Hollow Carbon Nanospheres as a High-Performance Anode Material for Potassium Ion Batteries. *J. Mater. Chem. A* **2018**, *6* (47), 24317–24323. https://doi.org/10.1039/C8TA09751H.

(19) Lu, J.; Wang, C.; Yu, H.; Gong, S.; Xia, G.; Jiang, P.; Xu, P.; Yang, K.; Chen, Q. Oxygen/Fluorine Dual-Doped Porous Carbon Nanopolyhedra Enabled Ultrafast and Highly Stable Potassium Storage. *Adv. Funct. Mater.* **2019**, *29* (49), 1906126. https://doi.org/10.1002/adfm.201906126.

(20) Jian, Z.; Luo, W.; Ji, X. Carbon Electrodes for K-Ion Batteries. *J. Am. Chem. Soc.* **2015**, *137* (36), 11566–11569. https://doi.org/10.1021/jacs.5b06809.

(21) Share, K.; Cohn, A. P.; Carter, R.; Rogers, B.; Pint, C. L. Role of Nitrogen-Doped Graphene for Improved High-Capacity Potassium Ion Battery Anodes. *ACS Nano* **2016**, *10* (10), 9738–9744. https://doi.org/10.1021/acsnano.6b05998.

(22) Zhang, Y.; Yang, L.; Tian, Y.; Li, L.; Li, J.; Qiu, T.; Zou, G.; Hou, H.; Ji, X. Honeycomb Hard Carbon Derived from Carbon Quantum Dots as Anode Material for K-Ion Batteries. *Mater. Chem. Phys.* **2019**, *229*, 303–309. https://doi.org/10.1016/j.matchemphys.2019.03.021.

(23) An, Y.; Fei, H.; Zeng, G.; Ci, L.; Xi, B.; Xiong, S.; Feng, J. Commercial Expanded Graphite as a Low–Cost, Long-Cycling Life Anode for Potassium–Ion Batteries with Conventional Carbonate Electrolyte. *J. Power Sources* **2018**, *378*, 66–72. https://doi.org/10.1016/j.jpowsour.2017.12.033.

(24) Liang, K.; Li, M.; Hao, Y.; Yan, W.; Cao, M.; Fan, S.; Han, W.; Su, J. Reduced Graphene Oxide with 3D Interconnected Hollow Channel Architecture as High-Performance Anode for Li/Na/K-Ion Storage. *Chem. Eng. J.* **2020**, *394*, 124956. https://doi.org/10.1016/j.cej.2020.124956.

(25) Liu, Y.; Fan, F.; Wang, J.; Liu, Y.; Chen, H.; Jungjohann, K. L.; Xu, Y.; Zhu, Y.; Bigio, D.; Zhu, T.; Wang, C. In Situ Transmission Electron Microscopy Study of Electrochemical Sodiation and Potassiation of Carbon Nanofibers. *Nano Lett.* **2014**, *14* (6), 3445–3452. https://doi.org/10.1021/nl500970a.

(26) Wang, X.; Han, K.; Qin, D.; Li, Q.; Wang, C.; Niu, C.; Mai, L. Polycrystalline Soft Carbon Semi-Hollow Microrods as Anode for Advanced K-Ion Full Batteries. *Nanoscale* **2017**, *9* (46), 18216–18222. https://doi.org/10.1039/C7NR06645G.

(27) Beda, A.; Rabuel, F.; Morcrette, M.; Knopf, S.; Taberna, P.-L.; Simon, P.; Matei Ghimbeu, C. Hard Carbon Key Properties Allow for the Achievement of High Coulombic Efficiency and High Volumetric Capacity in Na-Ion Batteries. *J. Mater. Chem. A* **2021**, *9* (3), 1743–1758. https://doi.org/c.

(28) Li, Z.; Zhang, J.; Guan, B.; Wang, D.; Liu, L.-M.; Lou, X. W. A Sulfur Host Based on Titanium Monoxide@carbon Hollow Spheres for Advanced Lithium–Sulfur Batteries. *Nat. Commun.* **2016**, *7* (1), 13065. https://doi.org/10.1038/ncomms13065.

(29) Yuan, X.; Zhu, B.; Feng, J.; Wang, C.; Cai, X.; Qin, R. Recent Advance of Biomass-Derived Carbon as Anode for Sustainable Potassium Ion Battery. *Chem. Eng. J.* **2021**, *405*, 126897. https://doi.org/10.1016/j.cej.2020.126897.

(30) Lu, Z.; Li, B.; Yang, D.; Lv, H.; Xue, M.; Zhang, C. A Self-Assembled Silicon/Phenolic Resin-Based Carbon Core–Shell Nanocomposite as an Anode Material for Lithium-Ion Batteries. *RSC Adv.* **2018**, *8* (7), 3477–3482. https://doi.org/10.1039/C7RA13580G.

(31) Jian, Z.; Xing, Z.; Bommier, C.; Li, Z.; Ji, X. Hard Carbon Microspheres: Potassium-Ion Anode Versus Sodium-Ion Anode. *Adv. Energy Mater.* **2016**, *6* (3), 1501874. https://doi.org/10.1002/aenm.201501874.

(32) Dahn, J. R.; Xing, W.; Gao, Y. The "Falling Cards Model" for the Structure of Microporous Carbons. *Carbon* **1997**, *35* (6), 825–830. https://doi.org/10.1016/S0008-6223(97)00037-7.

(33) Cowlard, F. C.; Lewis, J. C. Vitreous Carbon — A New Form of Carbon. *J. Mater. Sci.* **1967**, *2* (6), 507–512. https://doi.org/10.1007/BF00752216.

(34) Zhao, L.; Hu, Z.; Lai, W.; Tao, Y.; Peng, J.; Miao, Z.; Wang, Y.; Chou, S.; Liu, H.; Dou, S. Hard Carbon Anodes: Fundamental Understanding and Commercial Perspectives for Na-Ion Batteries beyond Li-Ion and K-Ion Counterparts. *Adv. Energy Mater.* **2021**, *11* (1), 2002704. https://doi.org/10.1002/aenm.202002704.

(35) Li, W.; Li, Z.; Zhang, C.; Liu, W.; Han, C.; Yan, B.; An, S.; Qiu, X. Hard Carbon Derived from Rice Husk as Anode Material for High Performance Potassium-Ion Batteries. *Solid State Ion.* **2020**, *351*, 115319. https://doi.org/10.1016/j.ssi.2020.115319.

(36) Chen, M.; Wang, W.; Liang, X.; Gong, S.; Liu, J.; Wang, Q.; Guo, S.; Yang, H. Sulfur/Oxygen Codoped Porous Hard Carbon Microspheres for High-Performance Potassium-Ion Batteries. *Adv. Energy Mater.* **2018**, *8* (19), 1800171. https://doi.org/10.1002/aenm.201800171.

(37) Maetz, A.; Delmotte, L.; Moussa, G.; Dentzer, J.; Knopf, S.; Ghimbeu, C. M. Facile and Sustainable Synthesis of Nitrogen-Doped Polymer and Carbon Porous Spheres. *Green Chem.* **2017**, *19* (9), 2266–2274. https://doi.org/10.1039/C7GC00684E.

(38) Ghimbeu, C. M.; Decaux, C.; Brender, P.; Dahbi, M.; Lemordant, D.; Raymundo-Piñero, E.; Anouti, M.; Béguin, F.; Vix-Guterl, C. Influence of Graphite Characteristics on the Electrochemical Performance in Alkylcarbonate LiTFSI Electrolyte for Li-Ion Capacitors and Li-Ion Batteries. *J. Electrochem. Soc.* **2013**, *160* (10), A1907–A1915. https://doi.org/10.1149/2.101310jes.

(39) Stanislaw, B.; Andrzej, S.; Maciej, P., L. R. Radovic. Chemistry and Physics of Carbon VL - 27 JO. Dekker, MARCEL DEKKER, INC. 2001, 126-21

(40) Bommier, C.; Surta, T. W.; Dolgos, M.; Ji, X. New Mechanistic Insights on Na-Ion Storage in Nongraphitizable Carbon. *Nano Lett.* **2015**, *15* (9), 5888–5892. https://doi.org/10.1021/acs.nanolett.5b01969.

(41) Beda, A.; Escamilla-Pérez, A. M.; Simonin, L.; Matei Ghimbeu, C. Vegetal-Extracted Polyphenols as a Natural Hard Carbon Anode Source for Na-Ion Batteries. *ACS Appl. Energy Mater.* **2022**, *5* (4), 4774–4787. https://doi.org/10.1021/acsaem.2c00215.

(42) Fujimoto, M.; Kano, A.; Nobuhiko, H. Negative-electrode active material for sodium-ion secondary battery, method for manufacturing said negative-electrode active material, and sodium-ion secondary battery, WO/2014/88723, 2014, 15.

(43) Conder, J.; Vaulot, C.; Marino, C.; Villevieille, C.; Ghimbeu, C. M. Chitin and Chitosan—Structurally Related Precursors of Dissimilar Hard Carbons for Na-Ion Battery. *ACS Appl. Energy Mater.* **2019**, *2* (7), 4841–4852. https://doi.org/10.1021/acsaem.9b00545.

(44) Matei Ghimbeu, C.; Górka, J.; Simone, V.; Simonin, L.; Martinet, S.; Vix-Guterl, C. Insights on the Na+ Ion Storage Mechanism in Hard Carbon: Discrimination between the Porosity, Surface Functional Groups and Defects. *Nano Energy* **2018**, *44*, 327–335. https://doi.org/10.1016/j.nanoen.2017.12.013.

(45) Brender, P.; Gadiou, R.; Rietsch, J.-C.; Fioux, P.; Dentzer, J.; Ponche, A.; Vix-Guterl, C. Characterization of Carbon Surface Chemistry by Combined Temperature Programmed Desorption with in Situ X-Ray Photoelectron Spectrometry and Temperature Programmed Desorption with Mass Spectrometry Analysis. *Anal. Chem.* **2012**, *84* (5), 2147–2153. https://doi.org/10.1021/ac102244b.

(46) Beda, A.; Vaulot, C.; Rabuel, F.; Morcrette, M.; Matei Ghimbeu, C. The Role of Specific and Active Surface Areas in Optimizing Hard Carbon Irreversible Capacity Loss in Sodium Ion Batteries. *Energy Adv.* **2022**, *1* (4), 185–190. https://doi.org/10.1039/D2YA00004K.

(47) Wang, J.; Polleux, J.; Lim, J.; Dunn, B. Pseudocapacitive Contributions to Electrochemical Energy Storage in TiO_2 (Anatase) Nanoparticles. *J. Phys. Chem. C* **2007**, *111* (40), 14925–14931. https://doi.org/10.1021/jp074464w.

(48) Liu, X.; Tao, H.; Tang, C.; Yang, X. Anthracite-Derived Carbon as Superior Anode for Lithium/Potassium-Ion Batteries. *Chem. Eng. Sci.* **2022**, *248*, 117200. https://doi.org/10.1016/j.ces.2021.117200.

(49) Xu, Y.; Zhang, C.; Zhou, M.; Fu, Q.; Zhao, C.; Wu, M.; Lei, Y. Highly Nitrogen Doped Carbon Nanofibers with Superior Rate Capability and Cyclability for Potassium Ion Batteries. *Nat. Commun.* **2018**, *9* (1), 1720. https://doi.org/10.1038/s41467-018-04190-z.

(50) Ferrari, A. C. Raman Spectroscopy of Graphene and Graphite: Disorder, Electron–Phonon Coupling, Doping and Nonadiabatic Effects. *Solid State Commun.* **2007**, *143* (1–2), 47–57. https://doi.org/10.1016/j.ssc.2007.03.052.

(51) Couzi, M.; Bruneel, J.-L.; Talaga, D.; Bokobza, L. A Multi Wavelength Raman Scattering Study of Defective Graphitic Carbon Materials: The First Order Raman Spectra Revisited. *Carbon* **2016**, *107*, 388–394. https://doi.org/10.1016/j.carbon.2016.06.017.

(52) Adams, R. A.; Syu, J.-M.; Zhao, Y.; Lo, C.-T.; Varma, A.; Pol, V. G. Binder-Free N- and O- Rich Carbon Nanofiber Anodes for Long Cycle Life K-Ion Batteries. *ACS Appl Matter.Interfaces*. 2017, 9 (21), 17872.

(53) Sun, Q.; Li, D.; Cheng, J.; Dai, L.; Guo, J.; Liang, Z.; Ci, L. Nitrogen-Doped Carbon Derived from Pre-Oxidized Pitch for Surface Dominated Potassium-Ion Storage. *Carbon* **2019**, *155*, 601–610. https://doi.org/10.1016/j.carbon.2019.08.059.

(54) Beda, A.; Taberna, P.-L.; Simon, P.; Matei Ghimbeu, C. Hard Carbons Derived from Green Phenolic Resins for Na-Ion Batteries. *Carbon* **2018**, *139*, 248–257. https://doi.org/10.1016/j.carbon.2018.06.036.

(55) Merlen, A.; Buijnsters, J.; Pardanaud, C. A Guide to and Review of the Use of Multiwavelength Raman Spectroscopy for Characterizing Defective Aromatic Carbon Solids: From Graphene to Amorphous Carbons. *Coatings* **2017**, *7* (10), 153. https://doi.org/10.3390/coatings7100153.

(56) Wang, B.; Zhang, Z.; Yuan, F.; Zhang, D.; Wang, Q.; Li, W.; Li, Z.; Wu, Y. A.; Wang, W. An Insight into the Initial Coulombic Efficiency of Carbon-Based Anode Materials for Potassium-Ion Batteries. *Chem. Eng. J.* **2022**, *428*, 131093. https://doi.org/10.1016/j.cej.2021.131093.

(57) Figueiredo, J. L.; Pereira, M. F. R.; Freitas, M. M. A.; Órfão, J. J. M. Modification of the Surface Chemistry of Activated Carbons. *Carbon* **1999**, *37* (9), 1379–1389. https://doi.org/10.1016/S0008-6223(98)00333-9.

(58) Zhang, B.; Ghimbeu, C. M.; Laberty, C.; Vix-Guterl, C.; Tarascon, J.-M. Correlation Between Microstructure and Na Storage Behavior in Hard Carbon. *Adv. Energy Mater.* **2016**, *6* (1), 1501588. https://doi.org/10.1002/aenm.201501588.

(59) Touja, J.; Gabaudan, V.; Farina, F.; Cavaliere, S.; Caracciolo, L.; Madec, L.; Martinez, H.; Boulaoued, A.; Wallenstein, J.; Johansson, P.; Stievano, L.; Monconduit, L. Self-Supported Carbon Nanofibers as Negative Electrodes for K-Ion Batteries: Performance and Mechanism. *Electrochimica Acta* **2020**, *362*, 137125. https://doi.org/10.1016/j.electacta.2020.137125.

(60) Wang, H.; Zhai, D.; Kang, F. Solid Electrolyte Interphase (SEI) in Potassium Ion Batteries. *Energy Environ. Sci.* **2020**, *13* (12), 4583–4608. https://doi.org/10.1039/D0EE01638A.

(61) Chen, C.; Wu, M.; Wang, Y.; Zaghib, K. Insights into Pseudographite-Structured Hard Carbon with Stabilized Performance for High Energy K-Ion Storage. *J. Power Sources* **2019**, *444*, 227310. https://doi.org/10.1016/j.jpowsour.2019.227310.

(62) Zhang, J.; Lai, L.; Wang, H.; Chen, M.; Shen, Z. X. Energy Storage Mechanisms of Anode Materials for Potassium Ion Batteries. *Mater. Today Energy* **2021**, *21*, 100747. https://doi.org/10.1016/j.mtener.2021.100747.

(63) Xu, J.; Fan, C.; Ou, M.; Sun, S.; Xu, Y.; Liu, Y.; Wang, X.; Li, Q.; Fang, C.; Han, J. Correlation between Potassium-Ion Storage Mechanism and Local Structural Evolution in Hard Carbon Materials. *Chem. Mater.* **2022**, *34* (9), 4202–4211. https://doi.org/10.1021/acs.chemmater.2c00646.

(64) Caracciolo, L.; Madec, L.; Gachot, G.; Martinez, H. Impact of the Salt Anion on K Metal Reactivity in EC/DEC Studied Using GC and XPS Analysis. *ACS Appl. Mater. Interfaces* **2021**, *13* (48), 57505–57513. https://doi.org/10.1021/acsami.1c19537.

(65) Saikia, D.; Wu, H.-Y.; Pan, Y.-C.; Lin, C.-P.; Huang, K.-P.; Chen, K.-N.; Fey, G. T. K.; Kao, H.-M. Highly Conductive and Electrochemically Stable Plasticized Blend Polymer Electrolytes Based on PVdF-HFP and Triblock Copolymer PPG-PEG-PPG Diamine for Li-Ion Batteries. *J. Power Sources* **2011**, *196* (5), 2826–2834. https://doi.org/10.1016/j.jpowsour.2010.10.096.

(66) Kubota, K.; Shimadzu, S.; Yabuuchi, N.; Tominaka, S.; Shiraishi, S.; Abreu-Sepulveda, M.; Manivannan, A.; Gotoh, K.; Fukunishi, M.; Dahbi, M.; Komaba, S. Structural Analysis of Sucrose-Derived Hard Carbon and Correlation with the Electrochemical Properties for Lithium, Sodium, and Potassium Insertion. *Chem. Mater.* **2020**, *32* (7), 2961–2977. https://doi.org/10.1021/acs.chemmater.9b05235.

(67) Li, Y.; Lu, Y.; Meng, Q.; Jensen, A. C. S.; Zhang, Q.; Zhang, Q.; Tong, Y.; Qi, Y.; Gu, L.; Titirici, M.; Hu, Y. Regulating Pore Structure of Hierarchical Porous Waste Cork-Derived Hard Carbon Anode for Enhanced Na Storage Performance. *Adv. Energy Mater.* **2019**, *9* (48), 1902852. https://doi.org/10.1002/aenm.201902852.

(68) Luan, Y.; Hu, R.; Fang, Y.; Zhu, K.; Cheng, K.; Yan, J.; Ye, K.; Wang, G.; Cao, D. Nitrogen and Phosphorus Dual-Doped Multilayer Graphene as Universal Anode for Full Carbon-Based Lithium and Potassium Ion Capacitors. *Nano-Micro Lett.* **2019**, *11* (1), 30. https://doi.org/10.1007/s40820-019-0260-6.

(69) Jian, Z.; Luo, W.; Ji, X. Carbon Electrodes for K-Ion Batteries. *J. Am. Chem. Soc.* **2015**, *137* (36), 11566–11569. https://doi.org/10.1021/jacs.5b06809.

(70) Larhrib, B.; Madec, L.; Monconduit, L.; Martinez, H. Optimized Electrode Formulation for Enhanced Performance of Graphite in K-Ion Batteries. *Electrochimica Acta* **2022**, *425*, 140747. https://doi.org/10.1016/j.electacta.2022.140747.

TOC graphic